Attributing past carbon fluxes to CO₂ and climate change: respiration 1 response to CO₂ fertilization shifts regional distribution of the carbon sink 2 3 Gregory R. Quetin^{1,2}, Caroline A. Famiglietti¹, Nathan C. Dadap¹, A. Anthony Bloom³, 4 Kevin W. Bowman^{3,4}, Noah S. Diffenbaugh^{1,5}, Junjie Liu^{3,6}, Anna T. Trugman², Alexandra 5 G. Konings^{1,5} 6 ¹Department of Earth System Science, Stanford University, Stanford, CA, USA 7 ²Department of Geography, University of California, Santa Barbara, CA, USA 8 9 ³Jet Propulsion Laboratory, California Institute of Technology, Pasadena, CA, USA ⁴Joint Institute for Regional Earth System Science and Engineering (JIFRESSE), University of 10 California, Los Angeles, CA, USA 11 ⁵Woods Institute for the Environment, Stanford University, Stanford, CA, USA 12 ⁶California Institute of Technology, Pasadena, CA, USA 13 14 Corresponding author: Gregory R. Quetin (gquetin@ucsb.edu) 15 16 **Key Points:** 17 A Bayesian data-fusion system was used to assimilate global observations to constrain 18 centennial carbon cycle model dynamics 19 The spatial variation of the carbon sink is shaped by how strongly increased plant growth 20 leads to increased plant and soil respiration 21 • Higher respiration losses in wet tropics offsets stronger plant growth there, resulting in a 22

stronger carbon sink in the temperate regions

Abstract

24

25

26

27

28

29

30

31

32

33

34

35

36

37

38

39

40

41

42

43

Over the past century, increased atmospheric CO₂ concentrations have enhanced photosynthesis through CO₂ fertilization across the globe. However, the increased growth has also led to greater respiration rates – both from vegetation (autotrophic respiration) and through the breakdown of plant litter and soil organic matter (heterotrophic respiration). The resulting change in carbon flux – and its spatial distribution – that can be attributed to increasing CO₂ and climate change remain unknown. We used the Carbon Data Model Framework (CARDAMOM), a model-data fusion system that assimilates global observations from satellites and other sources to create an ensemble of observationally-constrained carbon cycle representations, to determine the photosynthesis and respiration fluxes that can be attributed to increased atmospheric CO₂ and associated climate change from 1920-2015. Across the globe, the response of photosynthesis and respiration to atmospheric CO₂ dominates their response to climate alone. The regional distribution of the carbon sink attributable to climate change and CO₂ is strongly influenced by the 'loss ratio of carbon gained' – the fraction of enhanced photosynthesis that is lost to respiration. While the wet tropics' attributable photosynthesis flux is 1.4 times larger than that of the temperate region, the attributable flux of net carbon uptake is actually 1.25 larger in the temperate region, due to the wet tropics' greater heterotrophic respiration response to enhanced plant growth. At global scale, the loss ratio of carbon gained is 83±0.6%. Our results highlight the importance of the respiration responses to enhanced plant growth in regulating the land carbon sink.

44

Plain Language Summary

Earth's land areas have taken up a large amount of carbon from the atmosphere over the last century. However, exactly where, why, and by how much carbon uptake has increased is uncertain. We used a modeling system informed by global observations from satellites and elsewhere to quantify how the flows of carbon changed in response to the last century of increasing atmospheric CO₂. We found that increased photosynthesis stimulates greater ecosystem respiration, decreasing CO₂'s effect on net land carbon uptake. The fraction of increased photosynthesis that goes to respiration (rather than land carbon storage) varies by region and determines the location of the largest net land carbon uptake. Although it acts indirectly through changes in plant and soil carbon stocks, the respiration response to CO₂ was a dominant component of the land carbon cycle response to human-caused emissions of CO₂ and associated climate change.

1 Introduction

Human activity affects the global carbon cycle both directly (e.g., through land use change) and indirectly (primarily through changes in climate caused by greenhouse gas emissions). The resulting changes in climate affect the rate at which ecosystems grow and decompose. Increased atmospheric CO₂ concentrations associated with emissions also directly stimulate photosynthesis through so-called CO₂ fertilization (Walker et al., 2020). Taken together, CO₂ fertilization and climate change affect the net land carbon sink, which is the balance of photosynthesis (gross primary productivity, GPP), respiration, and disturbance fluxes (e.g. fire, land use change). This land sink in turn affects the amount of CO₂ remaining in the

70

71

72

73

74

75

76

77

78

79

80

81

82

83

84

85

86

87

88

89

90

atmosphere and thus the magnitude of associated future climate change. That is, a strong set of interacting feedbacks exists between climate, CO₂ concentrations, and the carbon cycle (Friedlingstein & Prentice, 2010). However, the magnitude of these feedbacks is uncertain, contributing to the large spread in predicted atmospheric CO₂ concentrations by 2100 for a given emissions scenario (Friedlingstein et al., 2014; Lovenduski & Bonan, 2017). A necessary starting point for constraining this uncertainty is understanding how climate change and CO₂ fertilization have each changed the historical carbon uptake.

Previous studies attributing historical changes in GPP have found that the effect of CO₂ fertilization dominates other processes such as climate change or land use change over the last century (Melnikova & Sasai, 2020; Piao et al., 2013; Schwalm et al., 2020). Accordingly, the effect of CO₂ fertilization on GPP, including its magnitude and spatial distribution, has been intensively studied, although the roles of tropical ecosystems, stand age, and nutrient limitations remain controversial (Chi et al., 2022; Ellsworth et al., 2017; Norby & Zak, 2011). How much the historical net terrestrial carbon uptake increased in response to the past rise in atmospheric CO₂ (or past climate change) is not just dependent on GPP but also depends on the response of respiration. Although there is little to no direct effect of atmospheric CO₂ concentrations on respiration rates, there is potential for an indirect effect (Kuzyakov et al., 2019): first, increased GPP due to CO₂ fertilization leads to increased plant growth, then the eventual decomposition of that increased plant matter increases litter and soil organic matter pools, thus enhancing heterotrophic respiration (R_h). That is, CO₂ used for photosynthesis has two possible fates: a) being respired back to the atmosphere, or b) being stored in the ecosystem's soil and carbon pools.

To understand carbon-climate feedbacks, we must understand how any enhanced carbon uptake is partitioned between respiration to the atmosphere and storage in the ecosystem. A single metric captures this partitioning: the proportion of enhanced GPP lost to respiration, instead of being stored in the ecosystem (hereafter, referred to as "the loss ratio of carbon gained"). At a single mature forest site in Australia, Jiang et al (2020) found a loss ratio value of 87%. It is unclear how this ratio varies across the globe, and if it has been as large across the history of anthropogenic CO₂ enhancement as it was in the Jiang et al (2020) study. It is also unclear how historical changes in respiration (and, relatedly GPP) in response to CO₂ enhancement have changed in the presence of climate change.

At global scales and over century-scale time periods, land surface models are one of the only tools for understanding how complex changes in climate and CO₂ fertilization affect the carbon balance of the terrestrial ecosystem. Yet several factors limit the utility of widely-used land surface model ensembles. First, in the absence of any information about the magnitude and distribution of carbon pools in the distant past, model ensembles generally use spin-up procedures to start long-term simulations with carbon pools in steady state (i.e. defined to have zero net carbon flux). This is unrealistic, because even pre-industrial era carbon fluxes were not at equilibrium (Bauska et al., 2015). The steady state starting conditions explain the overwhelming majority of inter-model variation in present-day net ecosystem production (Huntzinger et al., 2020; Schwalm et al., 2019). Second, model uncertainty (in either model structure or parameter choices) is a dominant source of variation in carbon cycle forecasts (Bonan & Doney, 2018) and hindcasts (Bonan et al., 2019) of net carbon fluxes. In particular, soil and carbon turnover times – which are intimately tied to respiration rates – are poorly constrained (Pugh et al., 2020; Shi et al., 2020; Wieder et al., 2018).

115

116

117

118

119

120

121

122

123

124

125

126

127

128

129

130

131

132

133

134

135

136

To address these challenges, we used a Bayesian carbon cycle model data-fusion system called the Carbon Data Model Framework (CARDAMOM). For each grid cell across the globe, CARDAMOM estimates the initial conditions, ecosystem parameters, and carbon pool histories that best match a suite of observations (Bloom et al., 2016; Bloom & Williams, 2015). These assimilated observations (and observationally constrained products) include global maps of solar-induced fluorescence (SIF), net biosphere exchange (NBE), leaf area index (LAI), soil organic matter, and biomass. In addition to determining optimal carbon cycle parameters at each grid cell that best match observations, the CARDAMOM framework systematically quantifies parameter uncertainty, a methodological step that is absent in the majority of global carbon cycle models. A key innovation between the CARDAMOM runs performed here and other prognostic modelling efforts (e.g. Chen et al., (2019)) is that CARDAMOM is constrained by estimates of the net biome exchange derived from atmospheric inversions. Combined with the model structure and other observations related to photosynthesis (e.g. LAI, SIF), the time series of this integrated flux can help to constrain the spatio-temporal variations in respiration fluxes that are otherwise relatively unknown. The use of NBE data has been shown to be particularly critical in constraining models, especially as model structural complexity increases (Famiglietti et al., 2021). These dynamic fluxes, combined with information about the amount of carbon in the ecosystem (biomass and soil organic carbon), provide a constraint on the carbon turnover times and their sensitivity to changes in temperature at each grid cell.

Although CARDAMOM contains only a single set of equations describing the carbon cycle, its flexibility to optimize parameters based on observations allows it to simulate a large range of possible flux dynamics with differing climatic sensitivities and growth patterns representative of variations within and across biomes globally. The flexibility in parameters

allows for similar carbon flux dynamics between CARDAMOM and more complex conventional land surface models (Quetin et al., 2020). This suggests that some of the uncertainty in CARDAMOM's model structure (i.e., carbon cycle equations) is accounted for through its explicit determination of parameter uncertainty, which is not accounted for in conventional land surface model ensembles. Thus, CARDAMOM systematically accounts for a range of carbon cycle uncertainty at each grid point while also balancing a large range of data from observations there in contrast to more complex models where spatial variation is more determined by broad categories of land cover types.

In this study, we used CARDAMOM to attribute what fraction of photosynthesis and respiration fluxes over the last century are due to climate change and to CO₂ fertilization, and constrain what proportion of enhanced GPP is lost to respiration instead of being stored in the terrestrial biosphere. We demonstrate that, across the globe, the loss ratio of carbon gained is large, significantly modulating the response of the net carbon balance to climate change and enhanced CO₂. We further demonstrate that variations in the loss ratio of carbon gained – rather than variations in carbon gain alone – significantly shift where the net land carbon sink has increased over the past century.

2 Methods

To study changes to the carbon cycle from 1920 - 2015, we combined contemporary (between 2000 - 2015) atmospheric and land surface observations with historical (1920 - 2015) climate forcing to constrain a mechanistic carbon cycle model through data assimilation. This data assimilation is described in Section 2.1. We then ran model experiments that isolate climate

change and rising CO₂ effects to attribute the carbon cycles response to each change individually and together (Section 2.2).

2.1 Retrieving carbon cycle parameters for the last century using model-data fusion

We used the CARDAMOM data assimilation framework and present-day global observations (between the years 2000 and 2015) to create a 1000 member ensemble of observationally constrained carbon cycle parameters and initial conditions (Bloom et al., 2016; Quetin et al., 2020). CARDAMOM was used to optimize the initial conditions of six carbon pools and one water pool, as well as 29 parameters that control the turnover rate, allocation, and environmental response of carbon and water in the Data Assimilation Linked Ecosystem Carbon v2.1.6

(DALECv2.1.6) carbon cycle model, which underlies the CARDAMOM model-data fusion system (Figure 1). The optimized parameters are listed in Supplementary Table 1.

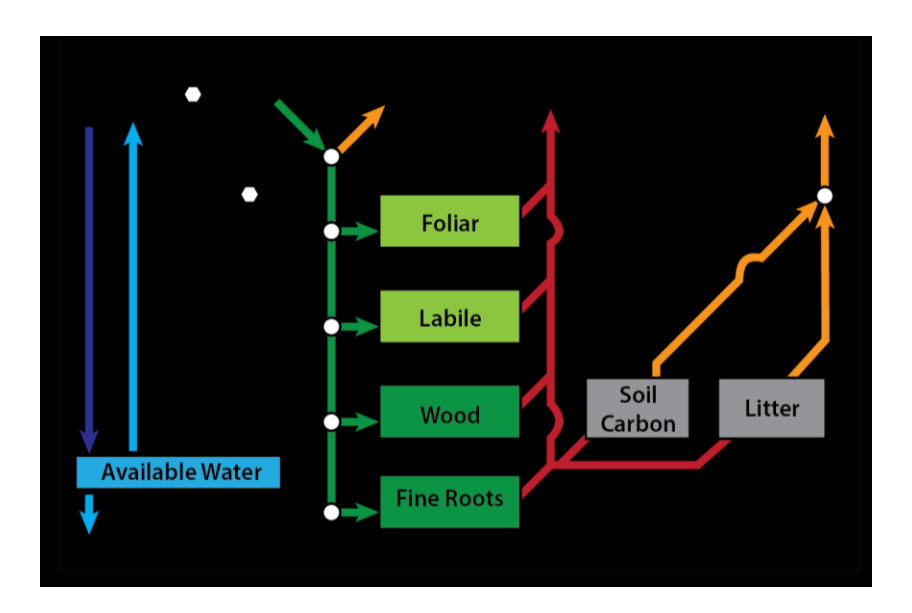


Figure 1: Diagram of the main components of DALECv2.1.6 used in CARDAMOM (reproduced from Quetin et al. (2020)).

The carbon cycle parameters and initial conditions (e.g., turnover times, photosynthesis sensitivities, etc.) that govern the response of the carbon cycle to increasing concentrations of CO₂ and climate change were retrieved using a data assimilation approach (further described in Section 2.1.3) such that model outputs best match observed data. These parameters and initial conditions were retrieved independently for each grid point, avoiding the need to assume that parameters only vary with plant functional type. This grid-point-by-grid-point retrieval approach is common in most other data assimilation systems (e.g. Smith et al. (2019)), and allows for the

estimation of parameter uncertainty (Butler et al., 2017). In particular, the Carbon Monitoring System Flux (CMS-Flux) – an atmospheric inversion estimate of net biosphere exchange using satellite observations of atmospheric concentrations of CO₂ – provided information on the carbon balance of the terrestrial ecosystem and constrained multiple aspects of the model (Liu et al., 2017, 2021).

2.1.1 Carbon cycle representation

The carbon cycle representation in DALEC is as described in Quetin et al. (2020) and Bloom et al., (2016), except for an alteration to the calculation of GPP and stomatal conductance. To improve the representation of the effect of CO₂ on stomatal conductance, we calculated leaf-level GPP and stomatal conductance using the coupled leaf photosynthesis-stomatal conductance models developed by Farquhar-Ball-Berry (Ball et al., 1987; Farquhar et al., 1980) and its analytical solution (Baldocchi, 1994) (see Supporting Information). This was a key update for representing centennial GPP and water use efficiency responses to climate change and the large rise in atmospheric CO₂ concentrations. As is common in land surface models incorporated in Earth system models, we scaled the leaf level results of GPP and stomatal conductance to the canopy as a single 'big leaf' with an exponential decay function of LAI (Sellers et al., 1992) (see Supporting Information). With this new model formulation, we also added an additional ecological dynamical constraint to those already contained in CARDAMOM (Bloom & Williams, 2015), that constrained the ratio of maximum carboxylation (V_{cmax25}) to the maximum

rate of whole chain electron transport at saturated light ($J_{\text{max}25})$ (see Supplementary Text S1) to

limit combinations that are not observed (Walker et al., 2014).

Table 1: Optimized parameters and initial conditions in CARDAMOM, corresponding flat prior ranges, and resulting state variables. Reproduced with modifications in bold in the "Ball Berry GPP" section from (Bloom et al., 2020; Quetin et al., 2020). Mean Temperature and Precipitation are represented by \bar{T} and \bar{P} respectively.

	Parameter	Description	Prior range
Allocation	Fauto	Autotrophic respiration	0.2 - 0.8
	Flab	NPP fraction to labile C	$0.01 - 0.5^*$
	Ffol	NPP fraction to foliar C	$0.01-0.5^*$
	froo	NPP fraction to fine root C	$0.01 - 0.5^*$
Allo iract	fwoo ¹	NPP fraction to stem C	$0.01 - 0.5^*$
	θwoo	Stem C turnover rate	$2.5 \times 10^{-5} - 10^{-3} day^{-1}$
Turnover rates	θ roo	Fine root C turnover rate	10 ⁻⁴ - 10 ⁻² day ⁻¹
	Θlit	Litter C turnover rate at \bar{T} , \bar{P}	10 ⁻⁴ - 10 ⁻² day ⁻¹
	θ som	Soil organic matter (SOM) turnover rate at \bar{T} , \bar{P}	10 ⁻⁷ - 10 ⁻³ day ⁻¹
	θ min	Mineralization of litter to SOM at \bar{T} , \bar{P}	10 ⁻⁵ - 10 ⁻² day ⁻¹
Ĕ	Θ	Heterotrophic temperature dependence factor	0.018 - 0.08
<u> </u>	Sp	Heterotrophic precipitation dependence factor	0.01 - 1
	d_{onset}	Leaf onset day	0 – 365.25
	$ m d_{fall}$	Leaf fall day	0 - 365.25
	c_{LMA}	Leaf C mass per area Leaf loss fraction	$5 - 200 \text{ g C m}^{-2}$
_	c _{ll}	Annual labile C release fraction	1/8 - 1 1/8 - 1
oby	c _{lr}	Labile release period	1/8 - 1 10 – 100 days
Canopy	$c_{ m ronset}$ $c_{ m rfall}$	Leaf fall period	20 – 150 days
	π_{foliar}^3	Combustion factors of foliar C	0.01 – 1
	π_{biomass}^{3}	Combustion factors of non-foliar biomass C	0.01 - 1 $0.01 - 1$
	π_{SOM}^3	Combustion factor of soil C	0.01 - 1
Fire	R	Resilience factor	0.01 - 1
<u> </u>	ω	Water stress threshold	$1-10^4 \text{ Kg H}_2\text{O m}^{-2}$
Water	α	³ Second order runoff decay constant	$3 \times 10^{-7} - 0.03 \text{ mm}^{-1} \text{ day}^{-1}$
Ma			
2.	$C_{lab}^{(t)}$	Labile C at time <i>t</i>	$1 - 2000 \text{ gC m}^{-2}$
	$\mathcal{C}_{fol}^{(t)}$	Foliar C at time t	$1 - 2000 \text{ gC m}^{-2}$
	$\mathcal{C}_{roo}^{(t)}$	Fine root C at time t	$1 - 2000 \text{ gC m}^{-2}$
bles	$C_{woo}^{(t)}$	Above- and below-ground woody C at time t	$1-10^5~{\rm gC~m^{-2}}$
aria	$C_{lit}^{(t)}$	Litter C at time <i>t</i>	$1-2000~gC~m^{-2}$
Ball Berry GPP State variables ²	$C_{som}^{(t)}$	Soil organic C at time t	$1 - 2 \times 10^5 \text{ gC m}^{-2}$
Stat	$W^{(t)}$	Plant-available water at time <i>t</i>	$1-10^4 \text{ mm}$
PP	V _{cmax25}	maximum carboxylation rate	10 – 400 umol m ⁻² s ⁻¹
S S	т	Maximum note of whole shair slastness to see a	(Walker et al., 2014)
ır	J_{max}	Maximum rate of whole chain electron transport	20 – 400 umol m ⁻² s ⁻¹
Be	m	at saturated light	(Walker et al., 2014)
3all	m _{stomata}	Stomatal conductance slope	2 – 30 (Oleson et al., 2010)
<u> </u>			2010)

bstomata	Stomatal conductance intercept	.0011 mol m ⁻² s ⁻¹
		(Oleson et al., 2010)
$\mathbf{g}_{\mathbf{b}}$	Leaf boundary layer conductance to CO2	$.4 - 10 \text{ mol m}^{-2} \text{ s}^{-1}$ (Martin
		et al., 1999)

 π_{biomass} and $\pi_{\text{foliar}} > \pi_{\text{SOM}}$

2.1.2 Assimilated Carbon Cycle Observations

Our whole assimilation run spanned 1920 – 2015, with assimilated observations from 2000 – 2015. All variables in Table 1 were optimized. The suite of observations (summarized in Table 1) was chosen to leverage new remote sensing observations of the global carbon cycle. A key set of assimilated observations is CMS-Flux net biome exchange (NBE), which was determined through atmospheric inversion (Bey et al., 2001; Liu et al., 2017, 2021). These NBE estimates had previously been used to better constrain global respiration fluxes (Konings et al., 2019), as well as the balance of photosynthesis and respiration across the tropics (Liu et al., 2017), and as emergent constraints on carbon-climate feedbacks (Barkhordarian et al., 2021), among others. Additional observations were derived from the following gridded datasets: remotely sensed solar induced fluorescence (SIF) as a proportional constraint for GPP (Bloom et al., 2020; Frankenberg et al., 2011), remotely sensed leaf area index (LAI) (Bi et al., 2015), remotely sensed carbon monoxide (CO) to constrain the fraction of carbon lost from pools due to fire (Bowman et al., 2017; Worden et al., 2017), remotely sensed total biomass (Carreiras et al.,

¹ fwoo is equivalent to 1 - fauto - ffol - flab

^{*}Prior ranges are conservative approximations, see Fox et al., (2009) and CARDAMOM sample code for details on sequential allocation fraction sampling in DALEC models.

^{214 &}lt;sup>2</sup>Only initial conditions (at time t=0) are optimized in DALECv2.1.6.

³Using the ecological and dynamical constraint approach (Bloom & Williams, 2015) we ensure that that π_{foliar}

2017; Saatchi et al., 2011), and soil organic matter from the Harmonized World Soil Database (HWSD) (Hiederer & Köchy, 2011).

The biomass and soil organic material observations were both drawn from a static map and assimilated in the year and/or month most representative of their observation (June of 2015 for biomass and the year 2000 for soil organic material) as in (Bloom et al., 2016; Quetin et al., 2020). By contrast, NBE and SIF were assimilated as monthly time series from 2010 – 2015 and LAI as the long term mean from 2010 – 2015. The CO observations constrain biomass burning emissions fractions (see Table 1). Each dataset was re-gridded to 4°x5° latitude/longitude on the Goddard Earth Observing System - Chem (GEOS-Chem) for consistency with the CMS-Flux estimates (see Table 2, Supporting Information Section S3). All CARDAMOM assimilation and forward runs (i.e., DALEC model runs with the retrieved optimal parameters) were also performed at this resolution.

Table 2. Observation-based datasets assimilated into the $4^{\circ}\times5^{\circ}$ CARDAMOM simulation. Adapted with modification from (Bloom et al., 2020; Quetin et al., 2020).

		, ,	
Observation	Years	Dataset description	Uncertainty ⁴
Leaf area index (LAI)	2010 - 2015	MODIS LAI retrievals ¹ .	±log(1.2)
Soil organic matter	2000	Soil C from harmonized	$\pm \log(1.5)$
(SOM)		world soils database	
		(HWSD) (Hiederer & Köchy,	
		2011)	
Above- and below-	2015	GLAS-informed biomass map	$\geq \pm \log(1.5)^{\text{see }3}$
ground biomass (ABGB)		(Carreiras et al., 2017; Saatchi	
		et al., 2011)	
Solar-induced	2010 - 2015	GOSAT retrievals of	$\pm \log(2)^{\text{see }2}$
Fluorescence (SIF)		fluorescence (Frankenberg et	
E. C (DD)	2010 2015	al., 2011) ²	1200/
Fire C emissions (BB)	2010 - 2015	4°×5° inverse estimates of fire	$\pm 20\%$
		C emissions (Bowman et al., 2017; Worden et al., 2017).	
Net Biosphere exchange	2010 - 2015		Seasonal=±0.05 g C/m²/d
(NBE) ⁵	2010 - 2013	derived 4°×5° inverse	Annual= ± 0.02 g C/m ² /d
(1,22)		delived i 5 iliverse	7 minuar = 0.02 g C/m / u

estimates of terrestrial NBE (Liu et al., 2017, 2021).

- Only mean 2010-2015 LAI is assimilated into CARDAMOM, in order to mitigate the influence of
- seasonal LAI retrieval biases (Bi et al., 2015).
- ²Time-resoved SIF is assimilated as a relative constraint on the temporal variability of GPP when
- temperatures are greater than 5°C and LAI is greater than 0.2.
- ³see ref (Bloom et al., 2016) for details on the uncertainty on ABGB.
- ⁴Uncertainties denoted as $\pm \log()$ indicates log-transformed model and observed quantities.
- ⁵The CMS-Flux NBE is spatially smoothed using a 3x3 gaussian smoother to reduce noise.

255

256

257

258

259

260

262

263

264

265

267

268

269

2.1.3 Data assimilation methodology

CARDAMOM parameter optimization was performed with Bayesian inference in which observations *O* are paired to model parameters, states, and fluxes (*y*) to form the likelihood function (Bloom et al., 2016, 2020; Bloom & Williams, 2015; Quetin et al., 2020). The likelihood probability function was calculated as the product of individual likelihoods:

$$P(\mathbf{0}|\mathbf{y}) = P_{LAI} P_{SOM} P_{ABGB} P_{SIF} P_{NBE} P_{CO}$$
 (1)

where P(O|y) was the likelihood of y given observations (O) and P_X was the probability of variable X given the observations of that variable (Table 2). This formulation assumes that the error between observations was independent. The P_{LAI} , P_{SOM} and P_{ABGB} , and P_{CO} were derived as (Bloom et al., 2020; Quetin et al., 2020):

$$P \propto e^{-\frac{1}{2}\sum_{i} \left(\frac{m_{i} - o_{i}}{\sigma_{i}}\right)^{2}} \tag{2}$$

where m_i and o_i corresponds to the i^{th} observation of the corresponding DALEC-modeled quantity and σ_i accounts for the combined effects of DALEC model structural error, model inputs, and observation errors. To better capture the interannual variability, P_{NBE} included

separate probability calculations with different uncertainty estimates for monthly and annual likelihoods and the units of SIF and GPP in P_{SIF} were normalized by the mean, such that GPP dynamics were constrained by SIF even though the units are not the same. Consistent with previous CARDAMOM runs (e.g. (Bloom et al., 2016, 2020; Quetin et al., 2020)), uncertainties were ultimately chosen manually based on expert experience of the underlying dataset and the impact on CARDAMOM's match to the observations. For example, the seasonal uncertainty of NBE is held within a reasonable range of observed uncertainty but small enough to induce a seasonal cycle in NBE. See Quetin et al. (2020) and included references for further details. Additionally, CARDAMOM applied 'ecological and dynamical constraints' that reduce equifinality (Huntzinger et al., 2017) by eliminating parameter combinations that may match observations despite limited ecological plausibility (Bloom & Williams, 2015).

Finally, we replaced the Adaptive Metropolis-Hastings Markov Chain Monte Carlo (MHMCMC) algorithm which was previously used in CARDAMOM (described in Bloom et al. (2020)) with a Differential Evolution Markov Chain Monte Carlo (DEMCMC) to sample P(y|O) (Braak, 2006) (Levine et al. 2022, in prep). The DEMCMC allowed for an order of magnitude increase in random starting points to avoid local minima and path dependency, while it also provided modest improvement in computation time. The DEMCMC produced similar results to

the MHMCMC algorithm in minimizing the mismatch between carbon cycle observations and model values.

2.1.4 Model inputs for assimilation and attribution

CARDAMOM requires external inputs for climate variables (insolation, precipitation, temperature, and vapor pressure deficit), atmospheric concentration of CO₂, and burned area. For the assimilation runs, the climate inputs were taken from monthly CRUNCEP v7 reanalysis, which was chosen primarily for being available for most of the past century. CRUNCEP v7 is a combined datasets of the Climate Research Unit (CRU) and reanalysis data from National Centers for Environmental Prediction (NCEP) (Viovy, 2018). The atmospheric concentrations of CO₂ were taken from the historical values of the globally-averaged annual means used by the Intergovernmental Panel on Climate Change with values for 2006 – 2015 taken from RCP8.5 scenario which include a rise in CO₂ of 98.6 ppm between 1920 and 2015 (Pachauri & Reisinger, 2008; Taylor et al., 2012).

CARDAMOM simulates fire fluxes based on burned area inputs and optimized emissions factors relating burned area to emission rates of CO and CO₂. These simulations are necessary to relate simulated net ecosystem productivity with observed net biome exchange (since the latter also accounts for fire fluxes). We used the Global Fire Emissions Database (GFED) V4.1s burned area to drive CARDAMOM during the observational period (1997 – 2015) (Randerson et al., 2017). Prior to the observational period, we synthesized burned area at each point for the last century by randomly resampling from the distribution of observed GFED V4.1s observations for a given month. This synthesized burned area contained the same variance as the observations and

did not have a long-term trend. We also investigated an empirical linkage between burned area and climate inputs but found the burned area synthesized from observations had less error relative to observed burned area in recent decades (not shown). Although we did not investigate fire specifically in this study, fire is accounted for implicitly in the carbon cycle data assimilation in CARDAMOM (Exbrayat et al., 2018).

2.2 Attributing Change in the Carbon Cycle

Our overall approach for attributing the carbon cycle response to different past environmental changes is illustrated in Figure 2. We ran factorial forcing scenarios that included different combinations of climate change and historically rising CO₂: i) historical climate change and increased atmospheric CO₂ concentrations, as during the assimilation stage (referred to as the 'Total' scenario); ii) a control climate – repeating 1920 CRUNCEP meteorology – and steady atmospheric concentrations of CO₂ equal to those in the 1920s ('Control' scenario); iii) a historically rising (enhanced) atmospheric concentration of CO₂ with a control climate ('eCO₂' scenario); and iv) a scenario with historical climate changes but constant CO₂ at 1920 levels ('Climate' scenario, i.e. without CO₂ fertilization). The burned area was left the same as the assimilation runs across experiments. These combined Total, Control, eCO₂, and Climate experiments are similar to the approach used in previous studies to diagnose climate-carbon feedbacks in C4MIP (Arora et al., 2020; Friedlingstein et al., 2014; Jones et al., 2016), thus

isolating the effect of CO₂ on plant physiology from the effect of climate change on the carbon cycle.

Attribution of change in carbon fluxes was then determined as the difference between the respective carbon fluxes of the forced scenarios ('Total','eCO₂', and 'Climate') minus the control run ('Control'). Throughout this manuscript, we denote the attributed change in a flux due to enhanced CO₂ as ΔX^{eCO2} , the attributed change in a flux to climate as $\Delta X^{climate}$, and the attributed change when they both are combined as ΔX^{total} . In each of the above cases, X denotes the carbon flux variable, such as GPP or R_h . For example, net ecosystem productivity due to enhanced CO₂ (ΔNEP^{eCO2}) is calculated as in Equation 3:

$$\Delta NEP^{eCO2} = NEP^{eCO2} - NEP^{Control} \tag{3}$$

= $NEP(control\ climate, historical\ CO_2) - NEP(control\ climate, control\ CO_2)$

Attribution was performed at each grid point on the cumulative sums from 1920 – 2015 and then spatially aggregated to calculate global and regional attribution, with regions defined as in Figure 3. The spatial aggregation method is discussed in Supplementary Text S2.

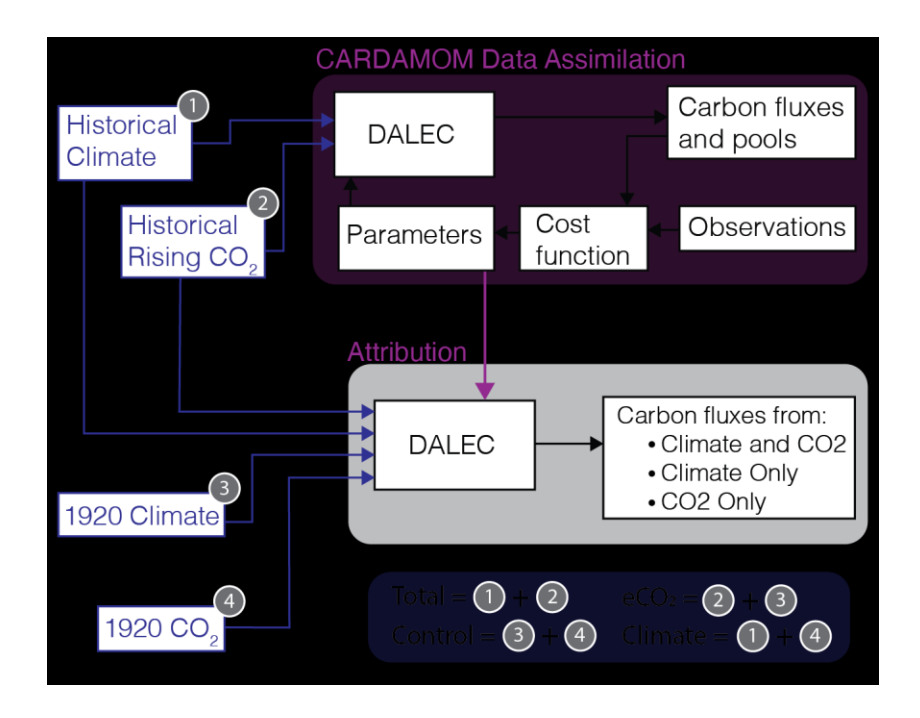


Figure 2: Summary of experimental design. We combine (pink) contemporary (2001-2016) atmospheric and land surface carbon cycle observations and historical climate forcing datasets (1920-2015) to constrain mechanistic carbon cycle responses to climate and atmospheric CO₂. Model runs (grey) forced by combinations of historical or control climate and CO₂ concentrations to create the 'Total', 'Control', 'eCO₂', and 'Climate' scenarios.

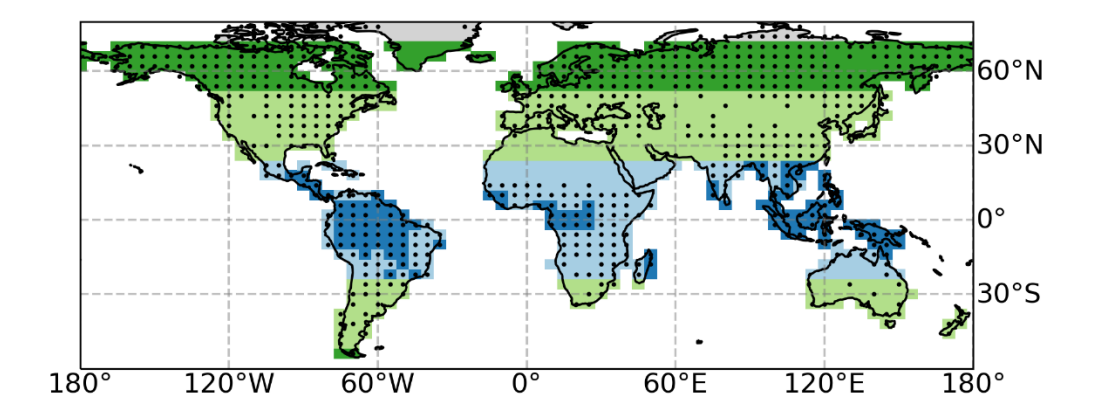


Figure 3: Regional divisions used for analysis. boreal (dark green), temperate (light green), wet tropics (blue), dry tropics (light blue). Black dots show points where CARDAMOM was able to complete the inversion (i.e. find a solution) in the simulated number of iterations.

3 Results and Discussion

3.1 Comparison of CARDAMOM simulations to assimilated estimates

We compared CARDAMOM to assimilated observations for verification, as well as to alternate independent modeled and observed estimates of the carbon cycle. Compared to assimilated observations, CARDAMOM has a strong match of the seasonal cycle of net biosphere exchange for all regions and a slightly muted interannual variation (Figure S1). Across space, the observations generally fall within CARDAMOM's uncertainty, although simulated leaf area is high and net biosphere exchange is somewhat lower than observations (that is, simulated uptake is higher than observed) around the equator. In the Sahel region, biomass is low and soil organic matter high relative to observations (Figure S2, Text S3). For the majority of

land points, CARDAMOM was able to retrieve a solution (Figure 3, black dots). Failed points primarily fell within the highly arid regions of the globe where there is relatively little carbon cycle activity. Some failed points may encompass regions important to the interannual variation of the carbon cycle (Poulter et al., 2014).

3.2 Comparison of CARDAMOM simulations to independent estimates

CARDAMOM's simulated carbon cycle dynamics are within range of several independent constraints that were not directly assimilated. The average global GPP from CARDAMOM (90 ± 1.3 Pg C/yr, $25\text{-}75^{th}$ percentile uncertainty for the period 2003 - 2015) is at the low end – but within the range of – several alternative estimates (Figure 4). CARDAMOM GPP are generally on the low end of other estimates in the tropical regions, while CARDAMOM GPP is more similar in both the seasonal cycle and mean annual value in the Boreal and Temperate regions (Figure S4). These alternative estimates include observations (i.e. optical retrievals from NIRv and δO^{18} ratios), an observationally-informed machine learning model (FLUXCOM), or model ensembles (i.e. the Multi-scale synthesis and Terrestrial Model Intercomparison Project (MsTMIP) and Trends in Net Land-Atmosphere Carbon Exchange (TRENDY V9), see Table S1 for list of models used) (Badgley et al., 2019; Friedlingstein et al., 2020; Huntzinger et al., 2013; Sitch et al., 2008; Welp et al., 2011).

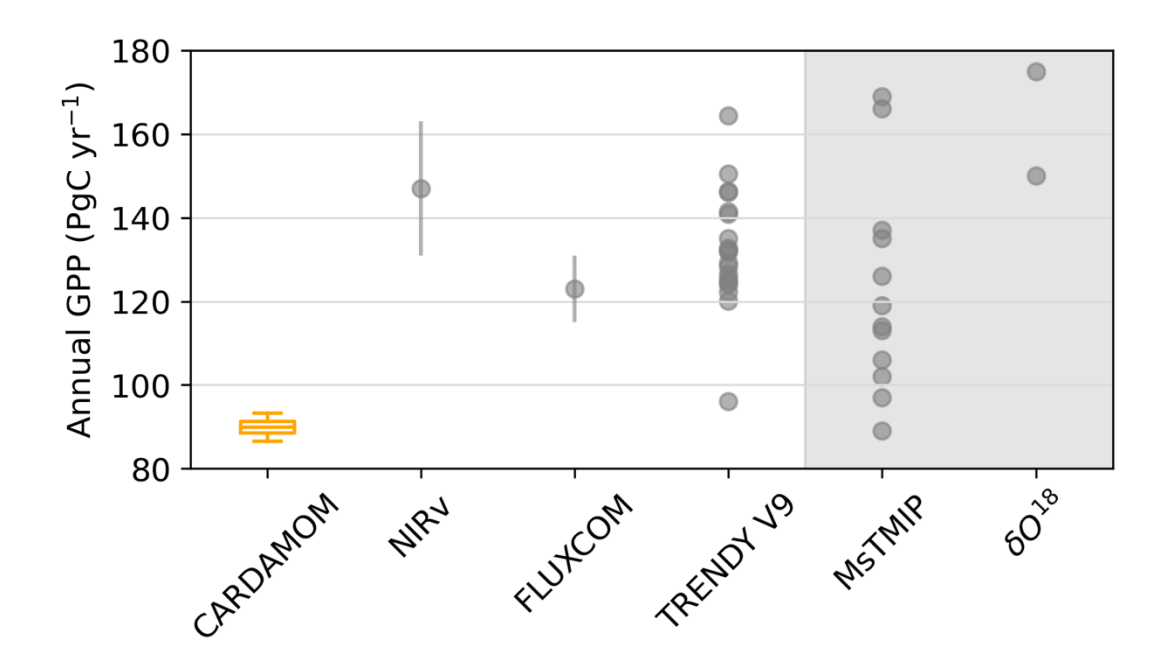


Figure 4: CARDAMOM mean annual Gross Primary Productivity (GPP, Pg C/yr) parameter ensemble spread with CRUNCEP climate 2003 – 2015 (Orange). Compared with observation-based estimates of global GPP from NIRv (2003 – 2015), FLUXCOM (2003 – 2015), and δO^{18} (1980 – 2010), and terrestrial biosphere estimates from TRENDY V9 (2003 – 2015), MsTMIP (2003 – 2010) (all in grey). Figure structure and data for NIRv, FLUXCOM, MsTMIP, and δO^{18} adapted from (Badgley et al., 2019). Whiskers of boxplot show δ^{th} – δ^{th} percentiles. Grey shading demarks literature values that do not directly overlap in time.

The zonal pattern of the apparent turnover time of the total ecosystem carbon for CARDAMOM (calculated using the total summed soil and vegetation carbon stocks, as in Fan et al. (2020)) is broadly similar to that of a recent observation-derived estimate of global turnover times for the same time span (Fan et al., (2020), which is an updated version of the estimate in Carvalhais et al. (2014)), at least between the latitudes of 46° S and 46° N (Figure 5). This is

reflected in the average values – 41 years for CARDAMOM and 30 years for that of Fan et al. (2020) (Figure 5). At high latitudes, however, the two estimates in Figure 5 diverge significantly, with CARDAMOM predicting a shorter turnover time. This divergence may relate to an underprediction of the size of soil carbon pools in CARDAMOM in regions with complex permafrost dynamics, since CARDAMOM does not have an explicit representation of the dynamics for permafrost and frozen soils. In addition, the soil organic matter estimates at high latitudes are highly uncertain because of the limited number of measurements. The HWSD soil organic matter dataset assimilated in CARDAMOM was shown to be on the low end of estimates in Fan et al. (2020), which would tend to drive CARDAMOM towards a shorter turnover time as well. Resolving this divergence and others illustrated above is likely to improve the accuracy and precision of carbon cycle analyses derived from CARDAMOM.

The difficulty in acquiring observations of soil carbon dynamics and their complexity makes the parameterization of turnover times in land surface models highly uncertain (Carvalhais et al., 2014; Friend et al., 2014; Koven et al., 2015), including at high latitudes (Koven et al., 2017). By contrast, the soil carbon turnover rates and initial carbon pool sizes in CARDAMOM are informed by observations of carbon fluxes and carbon states through data assimilation. The close match between the turnover times estimated by CARDAMOM and those estimated by observationally-driven and quasi-independent (some datasets included in Fan et al. (2020) are assimilated in CARDAMOM, some are not) values hints at the success of CARDAMOM's ability to accurately infer carbon cycle dynamics based on the assimilated observations.

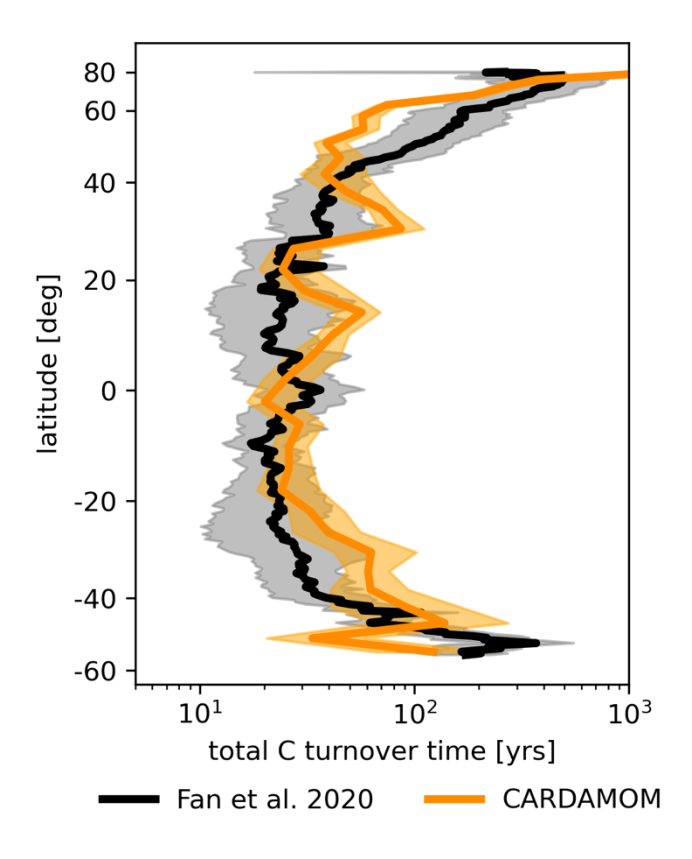


Figure 5: The zonally averaged turnover time for total ecosystem C in CARDAMOM (orange) compared to the quasi-independent estimates of Fan et al. 2020 (black), calculated between 2001 - 2014. Shading demarks $5^{th} - 95^{th}$ range of ensembles, solid line is median.

For more complete insight into the full historical dynamics simulated by CARDAMOM, we further compared it to independent model estimates of carbon flux timeseries from TRENDY V9 scenario 2 (change in climate and CO₂ but not land use change) (Figure 6, S3) and estimates of the sensitivity of GPP and NEP to increased CO₂ (Figure 7) (Friedlingstein et al., 2020). We find that the net primary productivity in the CARDAMOM 'Total' (Historical) run falls just below the TRENDY V9 set of models between 1920 and about 1980 (Figure 6). Up until 1960, CARDAMOM is a weak source to the atmosphere, while TRENDY V9 is neutral to a sink

440

441

442

443

444

445

446

447

448

449

450

451

452

453

454

455

456

457

458

throughout. These early differences highlight the difference in initial conditions between CARDAMOM and the models contained in TRENDY. While TRENDY models are run to equilibrium in 1700, CARDAMOM retrieves the initial carbon and water pools that serve to best match the observations assimilated. After 1980, the CARDAMOM Historical runs fall within the spread of models contained in TRENDY, ending in 2015 very close to the mean of the TRENDY models (Figure 6). This convergence in modern times may be due to the influence of similar observations on both models, which are systematically assimilated in CARDAMOM and assert influence over TRENDY as they are often used as validation. Like for NEP, the growth in CARDAMOM GPP since 1960 is much faster in CARDAMOM than in the TRENDY simulations (Figure S3), possibly due to analogous differences in initial condition parameterization and the influence of modern measurements. The relatively rapid CARDAMOM GPP growth compared to TRENDY is consistent with the results of Campbell et al. (2017), who used carbonyl sulfide records to show that historical GPP growth is higher than simulated by earth system models. During the period 1900 - 2013, GPP was estimated to grow by $31 \pm 5\%$, consistent with the $39 \pm 7\%$, simulated here during the slightly later period 1920 - 2015. As also shown in Fig. 4, the historical GPP simulated by CARDAMOM is lower than that simulated by the TRENDY models. Consistent with this pattern, autotrophic respiration is also lower than in the TRENDY models, while the heterotrophic respiration and LAI simulated by CARDAMOM are lower than most TRENDY models, but still fall within the low end of their range (Figure S3).

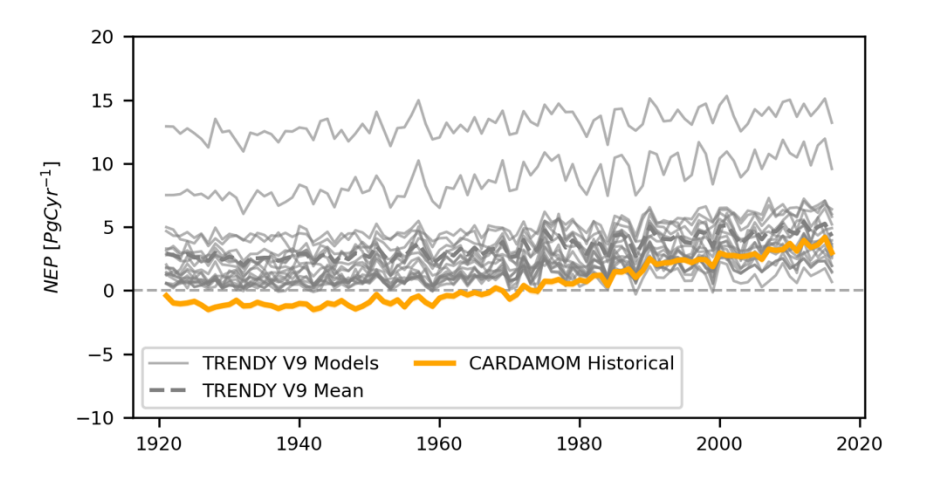


Figure 6: The annual timeseries of Net Ecosystem Productivity (NEP) from 1920 – 2015 from the CARDAMOM Historical run (orange, shading 5th – 95th percentile of ensemble), the individual TRENDY v9 models (grey solid) (Friedlingstein et al., 2020), and their multi-model mean (grey dashed). For a fair comparison, the global aggregation was performed only where there was a successful CARDAMOM run (black dots in Figure 3).

Lastly, because our study focused in part on the effect of historical atmospheric CO_2 increases on terrestrial carbon fluxes, we investigated whether the GPP and NEP CO_2 sensitivity calculated by CARDAMOM was in line with that of alternative estimates. Specifically, we calculated the CARDAMOM sensitivity of gross primary productivity as a percentage (β_{GPP}) and net ecosystem production (β_{NEP}) to enhanced CO_2 . The β_{GPP} and β_{NEP} were calculated by dividing the fractional gain of GPP or the carbon gained through NEP from 1920 – 2015 that was attributed to enhanced CO_2 by the change in atmospheric concentration of CO_2 over this period. Note that when calculating β_{GPP} , unlike when calculating β_{NEP} , the numerator was calculated as a percentage gain over 1920-2015 to facilitate comparison with literature values. Experimental manipulations in Free Air CO_2 Enrichment (FACE) studies provided observation-based but site-

478

479

480

481

482

483

484

485

486

487

488

489

490

491

492

493

494

495

496

497

498

499

specific estimates of relative GPP sensitivity to increased CO₂ (Hickler et al., 2008, p. 200), which cannot be directly compared to CARDAMOM because of its coarse resolution. Some differences in results between FACE studies and CARDAMOM would also be expected because of differences in the absolute atmospheric CO₂ levels between the two. Nevertheless, when considering CARDAMOM's relative GPP sensitivity to CO₂ across pixels, many pixels within the 5-95th percentile CARDAMOM range show the same sensitivity as observationally observed at four FACE experiments, which fall slightly below the 25th CARDAMOM percentile (Figure 7). Across the globe, model ensembles provide a further point of comparison. The GPP sensitivity to CO2 simulated by TRENDY V9 models and sampled at the CARDAMOM simulation points for 1920 - 2015 is generally considerably lower than that of CARDAMOM (Figure 7b). Like CARDAMOM's, the TRENDY GPP CO₂ sensitivity is also uncertain, both because of imperfect modelling assumptions and because no data are assimilated into TRENDY. It is thus difficult to ascertain whether or by how much CARDAMOM's GPP CO₂ sensitivity is too high or TRENDY's is too low. The relatively high CARDAMOM GPP sensitivity to CO₂ relative to that of conventional models is also reflected in the comparison between CARDAMOM NEP sensitivity to CO₂ and that of model intercomparisons, including estimates from TRENDY V9, which were regridded to

models is also reflected in the comparison between CARDAMOM NEP sensitivity to CO₂ and that of model intercomparisons, including estimates from TRENDY V9, which were regridded to CARDAMOM resolution and sampled where CARDAMOM provided a solution (black dots Figure 3), the Coupled Climate Carbon Cycle Model Intercomparison Project (C4MIP), and MsTMIP (Arora et al., 2013; Friedlingstein et al., 2006, 2020; Huntzinger et al., 2017) (Figure 7c). CARDAMOM's NEP sensitivity is on the high end of estimates from TRENDY and C4MIP, but in the middle of the range for MsTMIP. The different sensitivities exhibited by models from different intercomparison systems is reflective of their uncertainty. Nevertheless,

500	the differences between conventional model ensembles and CARDAMOM add a note of caution
501	to the results described in the manuscript.
502	Taken together, the reasonable – though imperfect – match between the CARDAMOM-
503	simulated historical carbon cycle (Figures 4-7, S3-S4) and independent estimates demonstrates
504	CARDAMOM's utility for process attribution of historical fluxes, as performed below.
505	
506	
507	
508	
509	
510	
511	
512	
513	

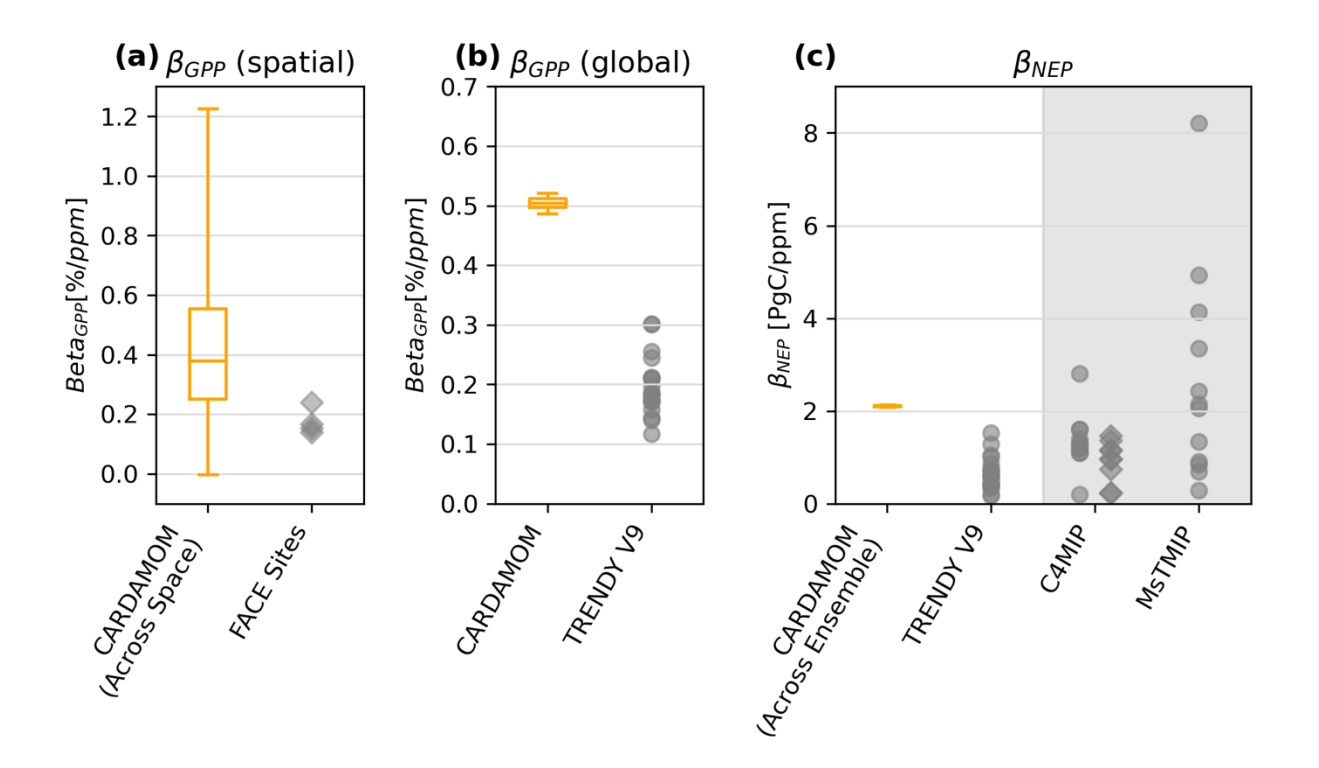


Figure 7: Comparison of the CARDAMOM mean sensitivity of carbon to eCO₂ for percent change in GPP with a) the CARDAMOM spread across space with FACE sites, b) CARDAMOM parameter spread of global mean with TRENDY V9 model spread. In c) the absolute change in NEP per change in ppm CO₂ for CARDAMOM simulations (orange, 1920 - 2015) including the ensemble uncertainty of the global mean and TRENDY V9 (1920 – 2015) models (Friedlingstein et al., 2020) and values drawn from literature for C4MIP (1901 – 2015) circles for (Friedlingstein et al., 2006, p. 20) and diamonds for (Arora et al., 2013) estimates, MsTMIP (1959 – 2010) from (Huntzinger et al., 2017) (all in grey). All CARDAMOM values are for 1920 – 2015 For a fair comparison, the global aggregation was performed only where there was a successful CARDAMOM run (black dots in Figure 3). Whiskers of boxplot show 5th – 95th percentiles. Grey shading demarks literature values that do not directly overlap in time.

3.3 Large gains in GPP under rising CO₂ are largely offset by the response of respiration to increased plant growth

528

529

530

531

532

533

534

535

536

537

538

539

540

541

542

543

544

545

546

547

548

549

550

Over the past century, the CARDAMOM simulations attribute large increases in global GPP to the combination of the historical enhanced atmospheric concentrations of CO₂ and climate change ($\Delta GPP^{total} = 1294 \pm 57$ Pg C, where the uncertainty is \pm the $25^{th} - 75^{th}$ range divided by two) (Figure 8). This modeled increase in global GPP is consistent with increasing GPP driving the satellite-observed greening of the Earth (Zhu et al., 2016). The increase in global GPP is primarily attributed to the GPP response to enhanced atmospheric concentrations of CO₂ ($\Delta GPP^{eCO2} = 974 \pm 76$ Pg C), which accounts for 75% of the total GPP change. The larger response to CO₂ than the response to climate is consistent with past studies using traditional model ensembles (Arora et al., 2013; Melnikova & Sasai, 2020; Piao et al., 2013; Schwalm et al., 2020), although this study is the first to quantify this effect using a dataconstrained methodology. Changes in climate over the past century have also impacted the carbon cycle. When only climate change is simulated, GPP decreases globally relative to the control experiment $(\Delta GPP^{Climate} = -551 \pm 72 \text{ Pg C})$. The negative response of GPP to the Climate only scenario is broadly consistent with negative responses of NPP seen in C4MIP experiments (Friedlingstein et

climate change is simulated, GPP decreases globally relative to the control experiment $(\Delta GPP^{Climate} = -551 \pm 72 \text{ Pg C})$. The negative response of GPP to the Climate only scenario is broadly consistent with negative responses of NPP seen in C4MIP experiments (Friedlingstein et al., 2006). Except under particularly hot conditions in the wet tropics, increased temperatures generally increase GPP by increasing chemical activity, but increased vapor pressure deficit reduces GPP by causing stomatal closure and reducing stomatal conductance (Fu et al., 2022). Overall, the potential benefits from warming due to climate change are offset by the effects of vapor pressure deficit-driven stomatal closure. (Note that changes in sunlight and precipitation were relatively small between 1920 – 2015, such that direct temperature and VPD effects were

the dominant climate drivers). This explains the global decrease in GPP in the climate change-only scenario. By contrast, the fact that Δ GPP is larger in the total scenario (Δ GPP^{total} = 1294 ± 57 Pg C) than in the enhanced CO₂-only scenario (Δ GPP^{eCO2} = 974 ± 76 Pg C) suggests that when CO2 and climate changes interact, climate has a positive (rather than negative as in Δ GPP^{Climate}) influence on the Total scenario. Under the increased CO₂ scenario, CO₂-induced stomatal closure limits the impact of vapor pressure deficit-induced stomatal closure. This is consistent with observations (Dusenge et al., 2019) and with the recognition that stomatal closure in response to enhanced CO₂ reduces evaporation (Lemordant et al., 2018; Swann et al., 2016). As a result, the direct positive effects of increasing temperature on GPP dominate, and the effect of climate change on GPP is positive. This coupling between the carbon-concentration and carbon-climate feedbacks allows climate changes to have a positive impact on GPP when increases in atmospheric CO₂ are present.

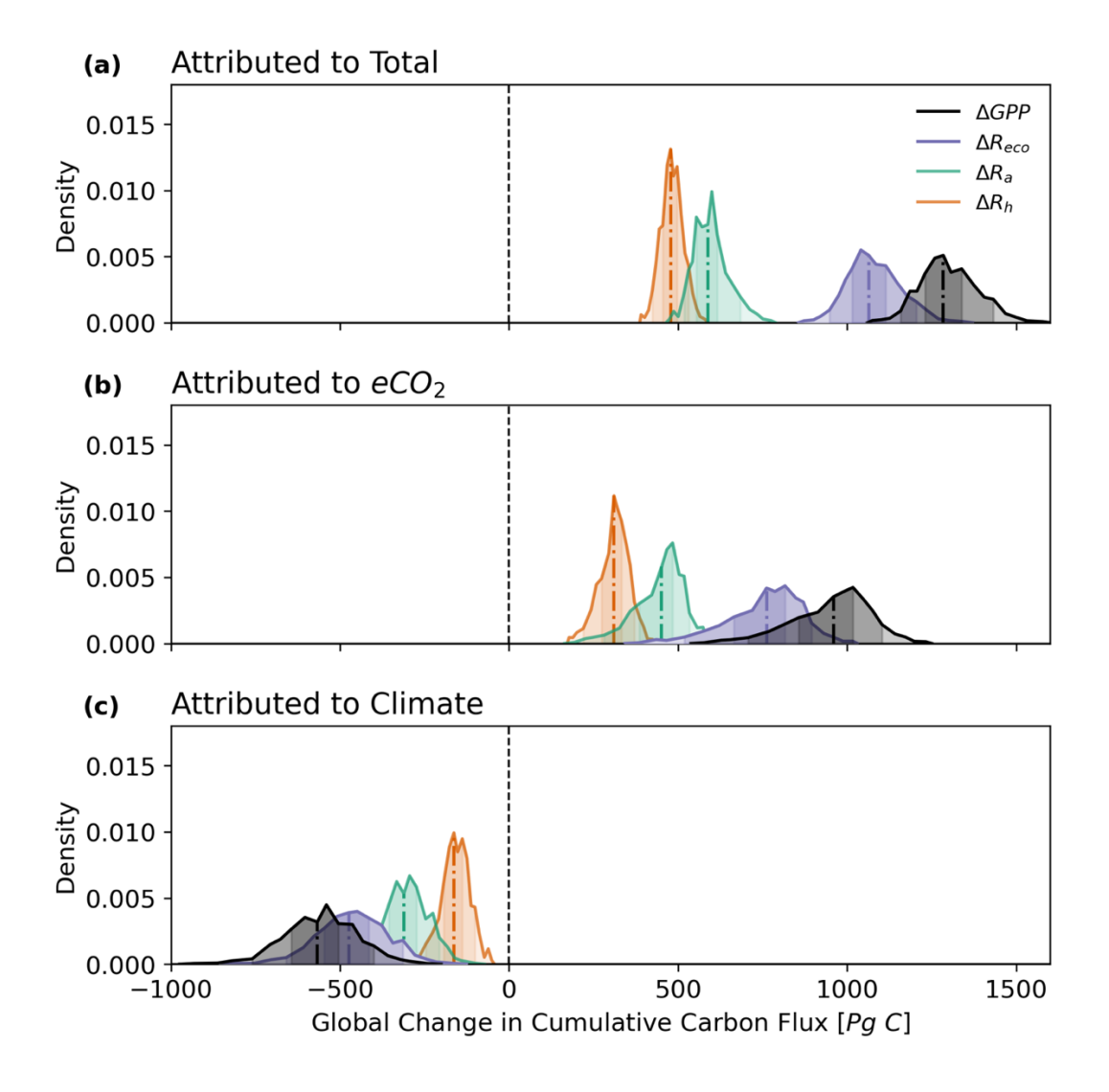


Figure 8: Magnitude of global cumulative sum of terrestrial carbon fluxes from 1920 - 2015 attributed to a) combined climate change and enhanced CO_2 ('Total' minus 'Control'), b) enhanced CO_2 alone ('e CO_2 ' minus 'Control'), and c) climate change alone ('Climate' minus 'Control'). Distributions for gross primary productivity (ΔGPP), ecosystem respiration (ΔR_{eco}), autotrophic respiration (ΔR_a), and heterotrophic respiration from litter and soils (ΔR_h) (Pg C). Colors per legend. The median of the whole distribution is shown as a colored dot-dashed line, while the percentiles of $5^{th} - 95^{th}$ and $25^{th} - 75^{th}$ percentile are shown as gradually darker shading. R_{eco} is equal to $R_h + R_a$.

The majority of the enhanced ecosystem respiration over the last century is due to a change in plant growth (i.e., input of additional carbon into the ecosystem), rather than an acceleration in the turnover of carbon due to the sensitivity to increasing temperature. Our analysis attributes a large increase of ecosystem respiration in response to the increased plant growth that occurs due to CO_2 fertilization. The majority of ΔGPP^{eCO_2} is lost to respiration $(\Delta R_{eco}^{eCO_2} = 774 \pm 72 \text{ Pg C})$ out of $\Delta GPP^{eCO_2} = 974 \pm 76 \text{ Pg C})$ (Figure 8). This increase in respiration is due to both autotrophic respiration $(\Delta R_a^{eCO_2} = 460 \pm 46 \text{ Pg C})$ and heterotrophic respiration $(\Delta R_h^{eCO_2} = 315 \pm 28 \text{ Pg C})$ rising significantly. This large respiration response to CO_2 -fertilization-driven increases in photosynthesis is consistent with observations at site-scale free-air carbon dioxide enrichment (FACE) studies, which have found that elevated atmospheric CO_2 concentrations lead to increases in soil respiration (King et al., 2004). By contrast, FACE studies find only mixed evidence for significant increases in soil organic matter (Hungate et al., 2009; Norby & Zak, 2011), which is consistent with our result that a large portion of stimulated photosynthesis is ultimately respired rather than stored in carbon pools.

The increase in respiration in the eCO₂ scenario ($\Delta R_{eco}^{eCO2} = 774 \pm 72$ Pg C) is large relative to that of the Total scenario ($\Delta R_{eco}^{total} = 1074 \pm 52$ Pg C), suggesting that most of the attributable respiration increase is due to increases in the magnitude of respiring carbon pools, rather than climate-driven increases in respiration rates. The importance of plant growth to changes in respiration over long periods of time in our experiments is consistent with observations of both a tight coupling between GPP and respiration across space and a strong relationship between interannual variations in GPP and respiration in flux tower observations (Baldocchi, 2008; Dusenge et al., 2019; Fernández-Martínez et al., 2014). The high respiration

response to plant growth is driven by both autotrophic ($\Delta R_a^{total} = 595 \pm 33 \text{ Pg C}$) and heterotrophic respiration ($\Delta R_h^{total} = 481 \pm 21 \text{ Pg C}$) in both the total and eCO₂ scenarios.

The dominance of the respiration response to carbon inputs alone, rather than to soil warming for example, highlights how the baseline (unmodified by climate) turnover times of different carbon pools play a large role in determining how much of the increased plant growth will stay in the ecosystem and the ultimate net carbon sink. These baseline turnover rates are set by many processes, including allocation of carbon between different plant pools with different respiration rates and microbial effects on heterotrophic respiration. This emphasizes the need for global carbon cycle studies to consider how the base turnover rates of different respiration pools are calibrated across the globe, not just their extensively-studied climatic sensitivities e.g. (Mahecha et al., 2010; Nottingham et al., 2020).

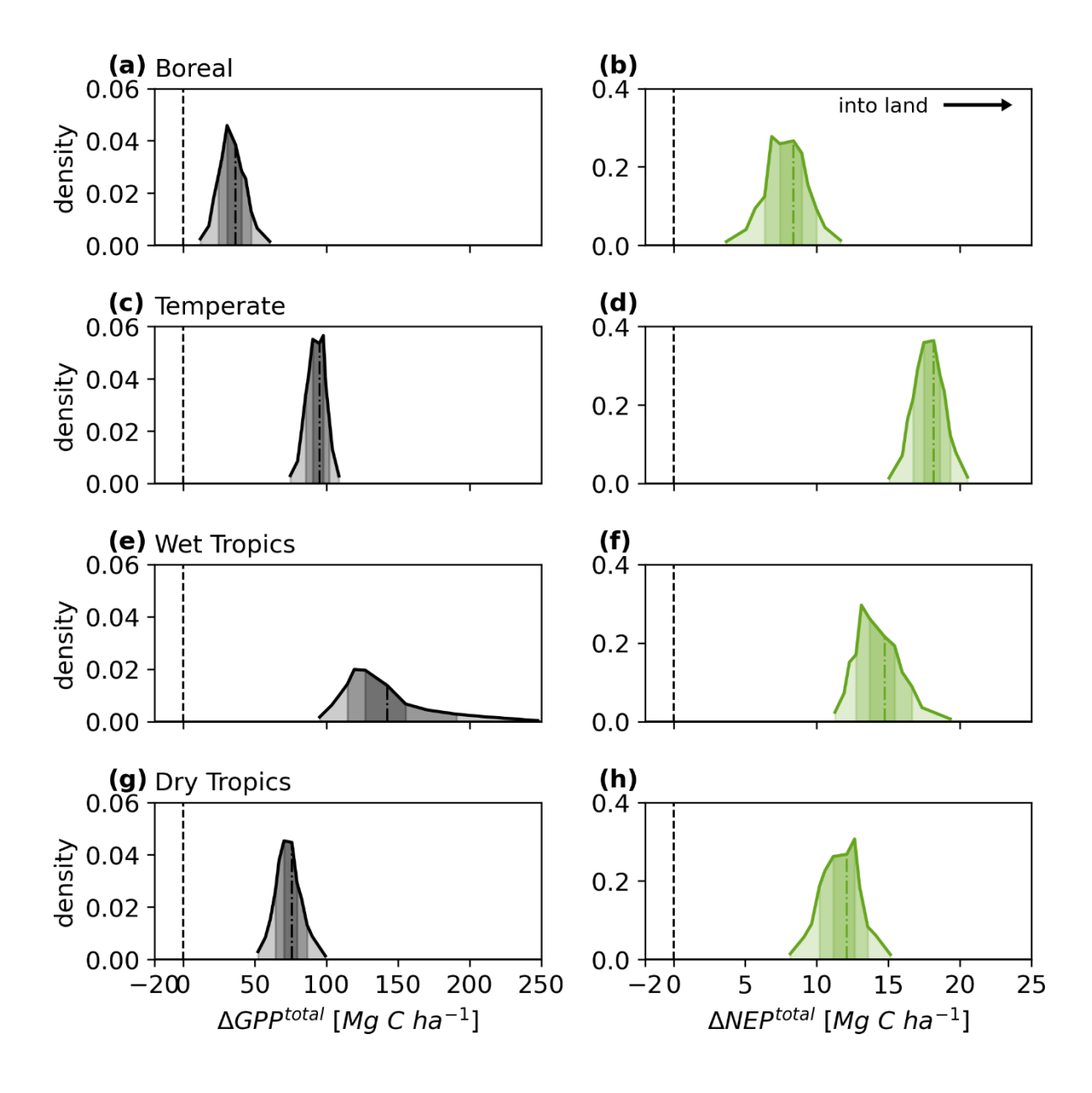


Figure 9: Distribution of cumulative per area change in $\triangle GPP^{total}$ (a, c, e, g) and $\triangle NEP^{total}$ (b, d, f, h). Note: NEP = -NEE. Carbon flux change by region attributed to the Total forcing (i.e., Total – Control) which includes both increasing CO_2 and changing climate. Darker shading corresponds to $5^{th} - 95^{th}$ percentile and $25^{th} - 75^{th}$ percentile of distributions due to both parameter and climate spread. Note that the y-axis is the same scale for all subplots in each

column.

3.4 Respiration response to CO₂ shapes regional balance of the net carbon flux

616

617

618

619

620

621

622

623

624

625

626

627

628

629

630

631

632

633

634

635

636

637

638

The changes in carbon sinks from rising CO₂ concentrations and changing climate vary across regions due to both spatial variation in enhanced carbon input (GPP) (Figure 9) and the respiration response. It is not surprising that the wet tropics, the region with the highest GPP on Earth (Badgley et al., 2019), also has the largest GPP increase due to enhanced CO₂. However, even though the greatest increase in ecosystem carbon input (GPP) is in the wet tropics, the total attributed ΔNEP^{total} is largest in the temperate region (17.8 ± 0.7 Mg C/ha). This increase in the temperate carbon sink per unit area is larger than that in the wet tropics (14.2 \pm 1.1 Mg C/ha), about twice as large as in the boreal (7.9 \pm 1.0 Mg C/ha) and in the dry tropics (11.6 \pm 0.9 Mg C/ha) (Figure 9). Thus, the net carbon sink in the temperate region has increased more than the net carbon sink in the wet tropics, despite GPP increasing more in the wet tropics (ΔGPP^{total} = 133.5 ± 15.5 Mg C/ha for wet tropics and $\Delta GPP^{total} = 92.8 \pm 4.6$ Mg C/ha for temperate). Independent atmospheric inversions for net carbon flux also find a strong carbon sink in the present-day temperate region compared to the nearly neutral tropics (Byrne et al., 2020; Gaubert et al., 2019). This geographic mismatch between the largest increase in GPP and largest increase in the carbon sink demonstrates the importance of respiration dynamics in determining the carbon balance of an ecosystem.

We can quantitatively summarize the response of the ecosystem to increased carbon input as the amount of new carbon lost compared to the increased carbon input, or the "loss ratio of carbon gained" ($\Delta R/\Delta GPP$). Note that the loss ratio of carbon gained is a distinct quantity from the ratio between total R_{eco} and GPP in historical fluxes (Baldocchi, 2008), as it reflects the response to added carbon input, rather than to total carbon input. As future ecosystem dynamics respond to climate change and increasing atmospheric CO₂ concentrations, the loss ratio of

carbon gained tracks how well they will serve as a sink in comparison to changes in carbon input. The $(\Delta R_{eco}/\Delta GPP)^{total}$ changes significantly across regions (Figure 10). It is highest in the wet tropics (89 ± 1%), where the highest portion of increased GPP is lost to respiration. It is lowest in the boreal region (76 ± 4%), such that more of the increased GPP remains stored in boreal ecosystems than in other regions. Both the temperate (81 ± 0.5%) and dry tropics (84 ± 1%) regions have values between the boreal and wet tropics. Across regions, the loss ratios of carbon gained in the Total scenarios are only a few percentage points larger than the equivalent values in the eCO₂ scenario, which does not experience climate change (Figure 10). The small change due to climate change shows that the loss ratio of carbon gained is primarily set by the base turnover rates in different regions, rather than changes in the turnover rates due to their climatic sensitivities.

The loss ratio of carbon gained due to heterotrophic respiration varies more between regions (e.g., from $44 \pm 1.5\%$ in the dry tropics to $24 \pm 3.4\%$ in the boreal) than that due to autotrophic respiration, which varies no more than 12 percentage points across regions (Figure 10). Thus, spatial variations in the loss ratio of carbon gained are primarily driven by spatial patterns of the heterotrophic respiration's loss ratio of carbon gained (i.e. $(\Delta R_h/\Delta GPP)^{total}$), rather than by that for autotrophic respiration (Figure 10). The higher heterotrophic respiration responses to enhanced CO_2 in tropical regions offsets the much larger response of GPP to CO_2 fertilization in the (wet) tropics, dropping the attributable net carbon flux below that of other regions. Note that our finding that the relatively large enhancements of CO_2 in the wet tropics translate to greater heterotrophic respiration fluxes is consistent with isotopic evidence from the flanks of two Costa Rican volcanoes, which are exposed to higher CO_2 concentrations. In these areas a strong relationship was found between trees with high xylem concentrations of CO_2 –

suggesting higher CO₂ fertilization – and higher nearby soil respiration fluxes (Bogue et al., 2019).

This study is the first to explicitly compare the amount of additional carbon fluxes across regions. The pattern of spatial variability in the loss ratio of carbon gained has significant consequences for the land carbon sink. While the increase in wet tropical GPP attributable to climate change and CO₂ is 1.4 – 4.0 times higher than in other regions, the high loss ratio of carbon gained causes the wet tropical gain in NEP to be only 0.8 – 1.8 times higher than that of other regions. This suggests a more limited regional importance for the wet tropics than would be apparent if only photosynthesis CO₂ fertilization rates were considered. Additionally, if it can be further supported, the finding of a particularly high respiration response to CO₂ fertilization in the wet tropics, driven by both soil and plant respiration rates, could be a useful constraint for understanding the net carbon flux of undisturbed tropical forests, particularly since they are under-represented in most in situ observational networks (Bond-Lamberty & Thomson, 2018; Jian et al., 2020; Schimel et al., 2015).

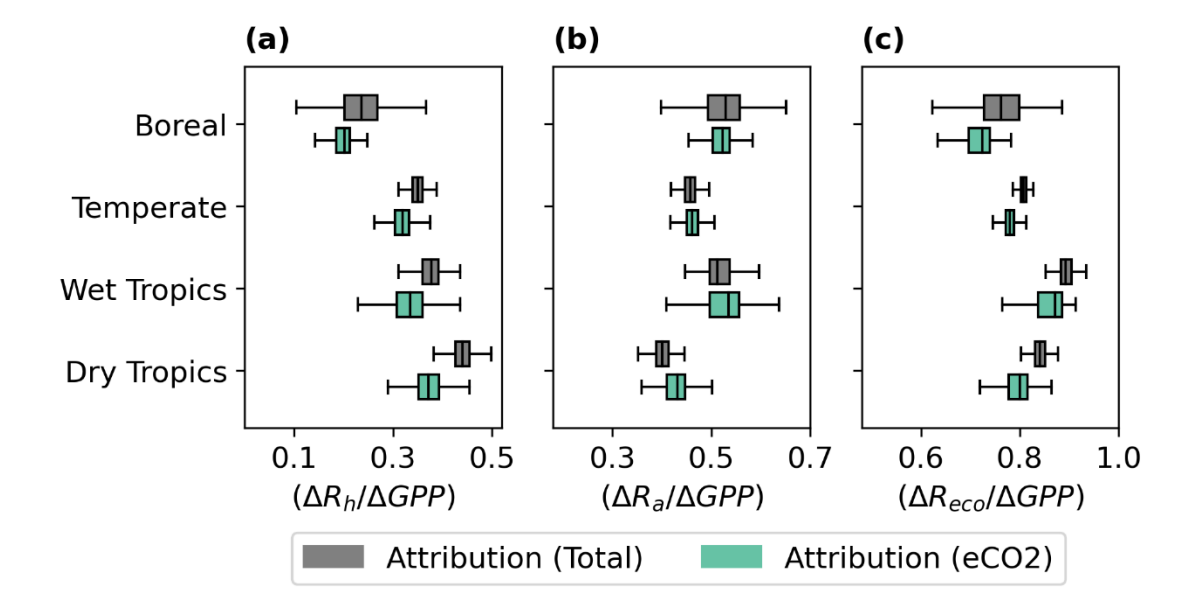


Figure 10: Ranges for the loss ratio of carbon gained ($\Delta R/\Delta GPP$) for a) heterotrophic respiration, b) autotrophic respiration, and c) ecosystem respiration. Larger values mean more carbon lost to the atmosphere. Gray denotes Total run minus Control and green denotes elevated CO_2 run minus Control. Vertical line is the median, colored box is the $25^{th}-75^{th}$ range, and whiskers are the 5^{th} to 95^{th} range. Note that the x-axis is not the same scale for all subplots.

3.5 Strong relationship between respiration and GPP constrained by observations

CARDAMOM-derived loss ratios of carbon gained show reasonably high overlap with those from land surface models included in the TRENDY V9 S2 experiment. This holds true for each of the cases where either the total, heterotrophic, or autotrophic respiration is considered – though TRENDY generally has a higher loss ratio of carbon gained for autotrophic respiration and thus total respiration (Figure 11). This similarity occurs despite the disagreement between CARDAMOM and TRENDY in the mean GPP magnitude and the sensitivity of GPP to increasing CO₂ (Figures 4, 7), and despite the very different inputs used to parameterize

CARDAMOM and TRENDY (i.e. parameters derived from observations in CARDAMOM, using plant functional types in TRENDY). This similarity is likely due to the similar process representations of carbon allocation and respiration in the two ensembles. However, the uncertainty across the TRENDY models is considerably larger than that of the observationally-constrained CARDAMOM ensemble.

The CARDAMOM loss ratio of carbon gained varies within a few percentage points at regional and global scales (Figures 10, 11). Put another way, there is a strong proportional relationship between the ΔGPP^{total} and the ΔR_{eco}^{total} , ΔR_{a}^{total} , and ΔR_{h}^{total} (as well as in the eCO₂ and Climate scenarios, not shown). This strong relationship echoes a previous finding by Hajima et al. (2014), who found a tightly constrained ratio of changes in heterotrophic respiration to net primary productivity in response to climate change and enhanced atmospheric concentrations of CO₂ in Earth System Models. Overall, the loss ratio of carbon gained may be a useful additional constraint on model representations of carbon cycle responses to global change, particularly given the large remaining uncertainties in the magnitude of global fluxes of respiration (Bond-Lamberty, 2018; Jian et al., 2022) and GPP (Badgley et al., 2019; Welp et al., 2011),.

Nevertheless, the tightly constrained nature and value of the loss ratio of carbon gained are subject to the uncertainties in the CARDAMOM system (as further discussed in Sec. 3.6 below) that will require further validation, ideally across different assimilation systems driven by observational data. These could include, e.g. other data assimilation systems (Fox et al., 2018; Peylin et al., 2016; Smith et al., 2020), or CARDAMOM runs with alternative observational constraints. For example, studies using radiocarbon have found that most carbon cycle models simulate unrealistically young median ages of soil C (Shi et al., 2020), suggesting our simulation and related studies would benefit from the explicit assimilation of radiocarbon observations.

Overall, as more and longer time series of observations become available, CARDAMOM and other data assimilation systems have the potential to further constrain the loss ratio of carbon gained.

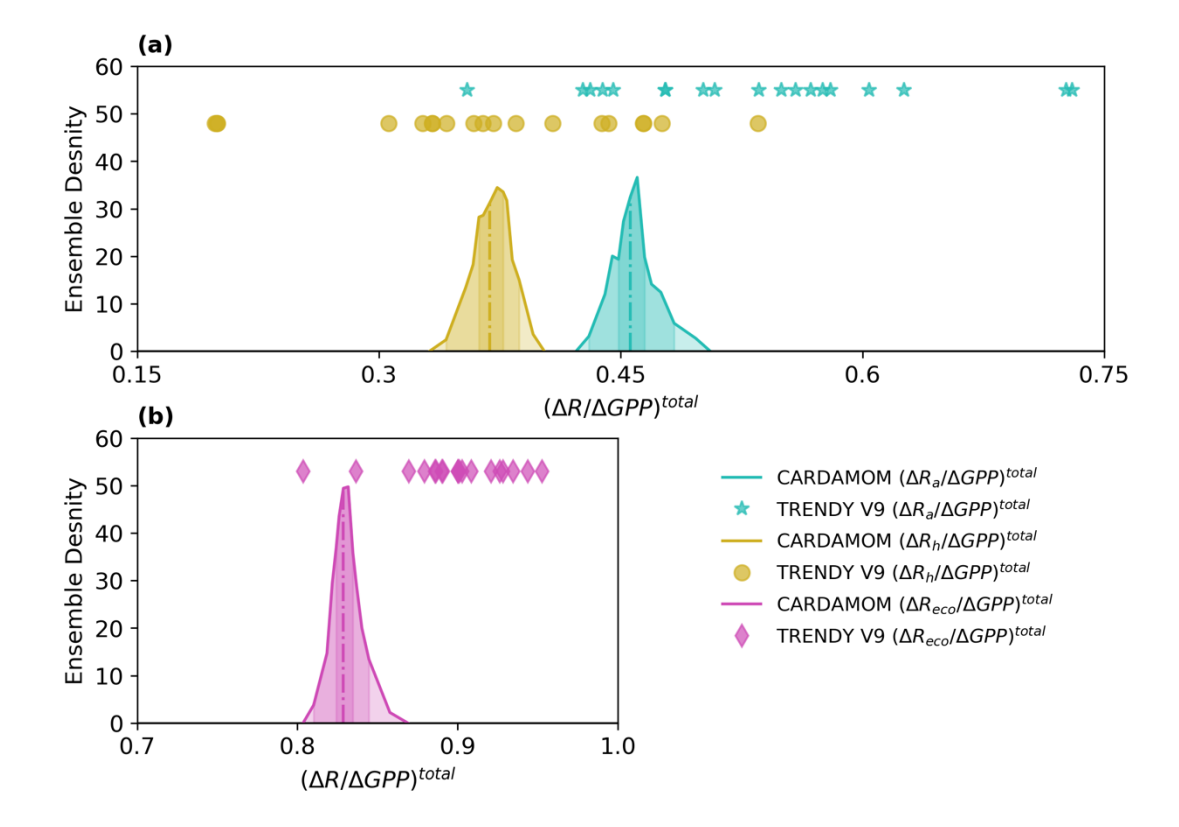


Figure 11: The global distributions of loss ratio of carbon gained ($\Delta R^{total}/\Delta GPP^{total}$) for a) heterotrophic respiration (R_h) and autotrophic respiration (R_a), and b) the ecosystem respiration (R_{eco}) over GPP. Points are the same ratio for individual TRENDY V9 models (Friedlingstein et al., 2020). Darker shading in the histograms for CARDAMOM distributions is for the $5^{th}-95^{th}$ and $25^{th}-75^{th}$ range. Note that the y-axis is the same scale for both subplots.

3.6 Uncertainties in CARDAMOM flux estimates

730

731

732

733

734

735

736

737

738

739

740

741

742

743

744

745

746

747

748

749

750

751

752

A number of relevant terrestrial carbon cycle processes are not explicitly represented in CARDAMOM, adding uncertainty to the above results. These include soil priming (van Groenigen et al., 2014), changes in microbial biomass (Wieder et al., 2013), lateral carbon flux (Regnier et al., 2013) and vegetation demography (Fisher et al., 2018). CARDAMOM uses relatively simplistic treatments of autotrophic respiration (proportional to photosynthesis with spatially variable carbon use efficiency) and heterotrophic respiration (using just two pools, litter and soil organic matter). Temporally variable nutrient limitations are also not represented, though spatial variability in nutrient limitations can be partially accounted for through reduced V_{cmax25} values. Past attribution studies using conventional model ensembles have found a significant effect from including the nitrogen cycle by lowering the carbon gained due to increased atmospheric concentrations of CO₂ (Huntzinger et al., 2017), lowering accumulation of soil carbon (Huntingford et al., 2022), and nutrient deposition impacts on photosynthesis (Schwalm et al., 2020). However, note that Chen et al. (2019) found that accounting for nitrogen deposition only mildly enhanced the simulated NEP since 1981 (Chen et al., 2019). Another key source of uncertainty in this study is the fact that CARDAMOM does not explicitly represent land use and land cover change (LULCC). Because a model without an explicit LULCC representation is assimilating observations that are influenced by the true historical LULCC, the CARDAMOM-retrieved parameters (and the associated carbon pools and fluxes) are likely to partially reflect historical LULCC. The lack of sub-grid scale heterogeneity in vegetation type in CARDAMOM makes it difficult to simulate LULCC. However, a sensitivity analysis can be performed by altering simulated burned area patterns to mimic land

cover changes due to LULCC. When tested for several representative locations, this sensitivity

analysis did not lead to any systematic change in the loss ratio of carbon gained, nor any other significant qualitative changes to the results discussed above (not shown). This suggests that the key qualitative conclusions of this manuscript are robust to LULCC effects, consistent with Schwalm et al. (2020), who found LULCC to be a relatively minor factor affecting GPP over the last century, and much smaller than CO₂ fertilization. Nevertheless, our sensitivity analyses were performed only on a small number of representative pixels and do not fully capture the potential effects of LULCC, which adds some uncertainty to our results.

CARDAMOM's advantage relative to conventional terrestrial biosphere model ensembles is not that it has an inherently more accurate ecosystem respiration representation, but that the observational constraints allow an exploration of the dynamics of carbon fluxes that is not dependent on *a priori* assumptions of the magnitude of the climatic sensitivities or base turnover times of various respiring carbon pools. Because dynamic net biome exchange and a snapshot of carbon stocks are assimilated into CARDAMOM (along with other observations such as SIF and LAI, and uncertainty accounting), turnover and respiration parameters can be explicitly constrained. This constraint is dependent in part on the observational uncertainty assumed. Although data assimilation systems can suffer from equifinality issues that can limit the utility of the assimilation outside the observational period, CARDAMOM's ecological and dynamic constraints (Bloom & Williams, 2015) and intermediate structural complexity (Famiglietti et al., 2021) help to reduce such equifinality. Thus, turnover should be more accurately constrained (see Figure 5) than in past prognostic models that use only information about vegetation states (e.g. Chen et al., (2019), Melnikova & Sesai, (2020)).

Despite the above limitations, previous research has shown that CARDAMOM is capable of representing ecosystem temporal dynamics similar to those of more structurally complex

conventional carbon cycle models (See Figure 6, 7 and 8 in Quetin et al. (2020)). In effect, CARDAMOM's explicit treatment of parameter uncertainty allows it to partially compensate for the added structural uncertainty compared to more complex models. As such, and based on the reasonable match to observations discussed in Text S3 and Sec 3.1, we expect the qualitative conclusions of our attribution calculations above to be robust.

4. Conclusions

We used data assimilation in CARDAMOM to attribute change in the terrestrial carbon cycle in response to enhanced atmospheric concentrations of CO₂ and climate change over the past century. Our analysis allowed for the retrieval of a parameters, including initial conditions, that are consistent with present-day observations of the carbon cycle at each grid point. This approach avoids the assumed spin-up to equilibrium that is common in other modeled projections of the carbon cycle, and estimates carbon cycle dynamics based on ecosystem observations rather than broad distributions of plant functional types.

The response of the carbon cycle is dominated by increased plant growth due to CO_2 fertilization across the globe and all regions. We identify the largest per area increase of GPP to be in the wet tropics, and the largest per area carbon sink to be in the temperate region. The location of the largest net carbon sink region per area is due the combination of large increases in plant growth with a relatively low 'loss ratio of carbon gained' in the temperate region compared to the more productive wet tropics. While the increase in wet tropical GPP is 1.4 - 4.0 times higher than in other regions, the wet tropical gain in NEP is only 0.8 - 1.8 times higher, because respiration fluxes are so much more responsive than in other regions even without considering changes in soil temperature.

The global loss ratio of carbon gained (globally, $83 \pm 0.6\%$) across the CARDAMOM ensemble's range of parameters is much less uncertain than the range of GPP increase, and accounts for the majority of increased productivity respired to the atmosphere. A significant portion of the loss ratio of carbon gained is due to heterotrophic respiration as a response to increased plant growth. This suggests that the base turnover rates of an ecosystem – rather than the sensitivity of those turnover rates to climate change – is the dominant driver of how much of and where the carbon fixed by enhanced CO_2 is stored in ecosystems under past and near-term climate change.

Acknowledgments, Samples, and Data

GRQ, KWB, AAB and AGK were supported by NASA NNH16ZDA001N-IDS. GRQ and AGK were also supported by NSF DEB-1942133. GRQ was also supported by NSF Grant 2003205.

NSD acknowledges support from Stanford University. Part of this work was carried out at the Jet Propulsion Laboratory, California Institute of Technology, under a contract with the National Aeronautics and Space Administration.

ATT acknowledges funding from the NSF Grants 2003205 and 2017949, the USDA National Institute of Food and Agriculture, Agricultural and Food Research Initiative Competitive Programme Grant No. 2018-67012-31496 and the University of California Laboratory Fees Research Program Award No. LFR-20-652467. All CARDAMOM datasets presented in this analysis are available on figshare (10.6084/m9.figshare.19952315, 10.6084/m9.figshare.19952246, 10.6084/m9.figshare.19951928), as well as the analysis script (10.6084/m9.figshare.21545547) and CARDAMOM code (10.6084/m9.figshare.21834501). All other datasets used are publicly available (see Methods).

823

References

846

825 Arora, V. K., Boer, G. J., Friedlingstein, P., Eby, M., Jones, C. D., Christian, J. R., et al. (2013). Carbon-826 Concentration and Carbon-Climate Feedbacks in CMIP5 Earth System Models. Journal of Climate, 827 26(15), 5289–5314. https://doi.org/10.1175/JCLI-D-12-00494.1 828 Arora, V. K., Katavouta, A., Williams, R. G., Jones, C. D., Brovkin, V., Friedlingstein, P., et al. (2020). Carbon-829 concentration and carbon-climate feedbacks in CMIP6 models and their comparison to CMIP5 models. Biogeosciences, 17(16), 4173–4222. https://doi.org/10.5194/bg-17-4173-2020 830 831 Badgley, G., Anderegg, L. D. L., Berry, J. A., & Field, C. B. (2019). Terrestrial gross primary production: Using 832 NIRV to scale from site to globe. Global Change Biology, gcb.14729. https://doi.org/10.1111/gcb.14729 833 Baldocchi, D. (1994). An analytical solution for coupled leaf photosynthesis and stomatal conductance models, 12. 834 Baldocchi, D. (2008). "Breathing" of the terrestrial biosphere: lessons learned from a global network of carbon 835 dioxide flux measurement systems. Australian Journal of Botany, 56(1), 1. 836 https://doi.org/10.1071/BT07151 837 Ball, J. T., Woodrow, I. E., & Berry, J. A. (1987). A Model Predicting Stomatal Conductance and its Contribution to 838 the Control of Photosynthesis under Different Environmental Conditions. In J. Biggins (Ed.), Progress in Photosynthesis Research (pp. 221–224). Springer Netherlands. Retrieved from 839 840 http://dx.doi.org/10.1007/978-94-017-0519-6 48 Barkhordarian, A., Bowman, K. W., Cressie, N., Jewell, J., & Liu, J. (2021). Emergent constraints on tropical 841 842 atmospheric aridity—carbon feedbacks and the future of carbon sequestration. Environmental Research 843 Letters, 16(11), 114008. https://doi.org/10.1088/1748-9326/ac2ce8 844 Bauska, T. K., Joos, F., Mix, A. C., Roth, R., Ahn, J., & Brook, E. J. (2015). Links between atmospheric carbon dioxide, the land carbon reservoir and climate over the past millennium. *Nature Geoscience*, 8(5), 383–387. 845

https://doi.org/10.1038/ngeo2422

847	Bey, I., Jacob, D. J., Yantosca, R. M., Logan, J. A., Field, B. D., Fiore, A. M., et al. (2001). Global modeling of
848	tropospheric chemistry with assimilated meteorology: Model description and evaluation. Journal of
849	Geophysical Research: Atmospheres, 106(D19), 23073-23095. https://doi.org/10.1029/2001JD000807
850	Bi, J., Knyazikhin, Y., Choi, S., Park, T., Barichivich, J., Ciais, P., et al. (2015). Sunlight mediated seasonality in
851	canopy structure and photosynthetic activity of Amazonian rainforests. Environmental Research Letters,
852	10(6), 064014. https://doi.org/10.1088/1748-9326/10/6/064014
853	Bloom, A. A., & Williams, M. (2015). Constraining ecosystem carbon dynamics in a data-limited world: integrating
854	ecological" common sense" in a model-data fusion framework. Biogeosciences, 12(5), 1299.
855	Bloom, A. A., Exbrayat, JF., Van Der Velde, I. R., Feng, L., & Williams, M. (2016). The decadal state of the
856	terrestrial carbon cycle: Global retrievals of terrestrial carbon allocation, pools, and residence times.
857	Proceedings of the National Academy of Sciences, 113(5), 1285–1290.
858	Bloom, A. A., Bowman, K. W., Liu, J., Konings, A. G., Worden, J. R., Parazoo, N. C., et al. (2020). Lagged effects
859	regulate the inter-annual variability of the tropical carbon balance. Biogeosciences, 17(24), 6393-6422.
860	https://doi.org/10.5194/bg-17-6393-2020
861	Bogue, R. R., Schwandner, F. M., Fisher, J. B., Pavlick, R., Magney, T. S., Famiglietti, C. A., et al. (2019). Plant
862	responses to volcanically elevated CO ₂ in two Costa Rican forests.
863	Biogeosciences, 16(6), 1343-1360. https://doi.org/10.5194/bg-16-1343-2019
864	Bonan, G. B., & Doney, S. C. (2018). Climate, ecosystems, and planetary futures: The challenge to predict life in
865	Earth system models. Science, 359(6375). https://doi.org/10.1126/science.aam8328
866	Bonan, G. B., Lombardozzi, D. L., Wieder, W. R., Oleson, K. W., Lawrence, D. M., Hoffman, F. M., & Collier, N.
867	(2019). Model Structure and Climate Data Uncertainty in Historical Simulations of the Terrestrial Carbon
868	Cycle (1850–2014). Global Biogeochemical Cycles, 33(10), 1310–1326.
869	https://doi.org/10.1029/2019GB006175
870	Bond-Lamberty, B. P. (2018). New Techniques and Data for Understanding the Global Soil Respiration Flux.
871	Earth's Future, 6(9), 1176–1180. https://doi.org/10.1029/2018EF000866
872	Bond-Lamberty, B. P., & Thomson, A. M. (2018). A Global Database of Soil Respiration Data, Version 4.0.
873	https://doi.org/10.3334/ORNLDAAC/1578

874	Bowman, K. W., Liu, J., Bloom, A. A., Parazoo, N. C., Lee, M., Jiang, Z., et al. (2017). Global and Brazilian
875	Carbon Response to El Niño Modoki 2011-2010: BRAZILIAN CARBON BALANCE. Earth and Space
876	Science, 4(10), 637-660. https://doi.org/10.1002/2016EA000204
877	Braak, C. J. F. T. (2006). A Markov Chain Monte Carlo version of the genetic algorithm Differential Evolution:
878	easy Bayesian computing for real parameter spaces. Statistics and Computing, 16(3), 239-249.
879	https://doi.org/10.1007/s11222-006-8769-1
880	Butler, E. E., Datta, A., Flores-Moreno, H., Chen, M., Wythers, K. R., Fazayeli, F., et al. (2017). Mapping local and
881	global variability in plant trait distributions. Proceedings of the National Academy of Sciences, 114(51),
882	E10937. https://doi.org/10.1073/pnas.1708984114
883	Byrne, B., Liu, J., Lee, M., Baker, I., Bowman, K. W., Deutscher, N. M., et al. (2020). Improved Constraints on
884	Northern Extratropical CO 2 Fluxes Obtained by Combining Surface-Based and Space-Based Atmospheric
885	CO 2 Measurements. Journal of Geophysical Research: Atmospheres, 125(15).
886	https://doi.org/10.1029/2019JD032029
887	Campbell, J. E., Berry, J. A., Seibt, U., Smith, S. J., Montzka, S. A., Launois, T., et al. (2017). Large historical
888	growth in global terrestrial gross primary production. Nature, 544(7648), 84-87.
889	Carreiras, J. M. B., Quegan, S., Le Toan, T., Ho Tong Minh, D., Saatchi, S. S., Carvalhais, N., et al. (2017).
890	Coverage of high biomass forests by the ESA BIOMASS mission under defense restrictions. Remote
891	Sensing of Environment, 196, 154-162. https://doi.org/10.1016/j.rse.2017.05.003
892	Carvalhais, N., Forkel, M., Khomik, M., Bellarby, J., Jung, M., Migliavacca, M., et al. (2014). Global covariation of
893	carbon turnover times with climate in terrestrial ecosystems. <i>Nature</i> , 514(7521), 213–217.
894	https://doi.org/10.1038/nature13731
895	Chen, J. M., Ju, W., Ciais, P., Viovy, N., Liu, R., Liu, Y., & Lu, X. (2019). Vegetation structural change since 1981
896	significantly enhanced the terrestrial carbon sink. Nature Communications, 10(1), 4259.
897	https://doi.org/10.1038/s41467-019-12257-8
898	Chi, C., Riley William J., Prentice I. Colin, & Keenan Trevor F. (2022). CO2 fertilization of terrestrial
899	photosynthesis inferred from site to global scales. Proceedings of the National Academy of Sciences,
900	119(10), e2115627119. https://doi.org/10.1073/pnas.2115627119

901	Dusenge, M. E., Duarte, A. G., & Way, D. A. (2019). Plant carbon metabolism and climate change: elevated CO2
902	and temperature impacts on photosynthesis, photorespiration and respiration. New Phytologist, 221(1), 32-
903	49. https://doi.org/10.1111/nph.15283
904	Ellsworth, D. S., Anderson, I. C., Crous, K. Y., Cooke, J., Drake, J. E., Gherlenda, A. N., et al. (2017). Elevated
905	CO2 does not increase eucalypt forest productivity on a low-phosphorus soil. Nature Climate Change, 7(4)
906	279–282. https://doi.org/10.1038/nclimate3235
907	Exbrayat, J., Smallman, T. L., Bloom, A. A., Hutley, L. B., & Williams, M. (2018). Inverse Determination of the
908	Influence of Fire on Vegetation Carbon Turnover in the Pantropics. Global Biogeochemical Cycles.
909	https://doi.org/10.1029/2018GB005925
910	Famiglietti, C. A., Smallman, T. L., Levine, P. A., Flack-Prain, S., Quetin, G. R., Meyer, V., et al. (2021). Optimal
911	model complexity for terrestrial carbon cycle prediction. Biogeosciences, 18(8), 2727–2754.
912	https://doi.org/10.5194/bg-18-2727-2021
913	Fan, N., Koirala, S., Reichstein, M., Thurner, M., Avitabile, V., Santoro, M., et al. (2020). Apparent ecosystem
914	carbon turnover time: uncertainties and robust features. Earth System Science Data, 12(4), 2517-2536.
915	https://doi.org/10.5194/essd-12-2517-2020
916	Farquhar, G. D., von Caemmerer, S., & Berry, J. A. (1980). A biochemical model of photosynthetic CO2
917	assimilation in leaves of C3 species. Planta, 149(1), 78-90. https://doi.org/10.1007/BF00386231
918	Fernández-Martínez, M., Vicca, S., Janssens, I. A., Sardans, J., Luyssaert, S., Campioli, M., et al. (2014). Nutrient
919	availability as the key regulator of global forest carbon balance. Nature Clim. Change, 4(6), 471-476.
920	Fisher, R. A., Koven, C. D., Anderegg, W. R. L., Christoffersen, B. O., Dietze, M. C., Farrior, C. E., et al. (2018).
921	Vegetation demographics in Earth System Models: A review of progress and priorities. Global Change
922	Biology, 24(1), 35-54. https://doi.org/10.1111/gcb.13910
923	Fox, A. M., Hoar, T. J., Anderson, J. L., Arellano, A. F., Smith, W. K., Litvak, M. E., et al. (2018). Evaluation of a
924	Data Assimilation System for Land Surface Models Using CLM4.5. Journal of Advances in Modeling
925	Earth Systems, 10(10), 2471–2494. https://doi.org/10.1029/2018MS001362
926	Frankenberg, C., Fisher, J. B., Worden, J., Badgley, G., Saatchi, S. S., Lee, JE., et al. (2011). New global
927	observations of the terrestrial carbon cycle from GOSAT: Patterns of plant fluorescence with gross primary
928	productivity. Geophysical Research Letters, 38(17).

929	Friedlingstein, P., & Prentice, I. C. (2010). Carbon–climate feedbacks: a review of model and observation based
930	estimates. Current Opinion in Environmental Sustainability, 2(4), 251–257.
931	Friedlingstein, P., Cox, P., Betts, R., Bopp, L., von Bloh, W., Brovkin, V., et al. (2006). Climate-Carbon Cycle
932	Feedback Analysis: Results from the C4MIP Model Intercomparison. Journal of Climate, 19(14), 3337-
933	3353. https://doi.org/10.1175/JCLI3800.1
934	Friedlingstein, P., Meinshausen, M., Arora, V. K., Jones, C. D., Anav, A., Liddicoat, S. K., & Knutti, R. (2014).
935	Uncertainties in CMIP5 Climate Projections due to Carbon Cycle Feedbacks. Journal of Climate, 27(2),
936	511–526. https://doi.org/10.1175/JCLI-D-12-00579.1
937	Friedlingstein, P., O'Sullivan, M., Jones, M. W., Andrew, R. M., Hauck, J., Olsen, A., et al. (2020). Global Carbon
938	Budget 2020. Earth System Science Data, 12(4), 3269-3340. https://doi.org/10.5194/essd-12-3269-2020
939	Friend, A. D., Lucht, W., Rademacher, T. T., Keribin, R., Betts, R., Cadule, P., et al. (2014). Carbon residence time
940	dominates uncertainty in terrestrial vegetation responses to future climate and atmospheric CO2.
941	Proceedings of the National Academy of Sciences, 111(9), 3280–3285.
942	https://doi.org/10.1073/pnas.1222477110
943	Fu, Z., Ciais, P., Prentice, I. C., Gentine, P., Makowski, D., Bastos, A., et al. (2022). Atmospheric dryness reduces
944	photosynthesis along a large range of soil water deficits. Nature Communications, 13(1), 989.
945	https://doi.org/10.1038/s41467-022-28652-7
946	Gaubert, B., Stephens, B. B., Basu, S., Chevallier, F., Deng, F., Kort, E. A., et al. (2019). Global atmospheric CO2
947	inverse models converging on neutral tropical land exchange, but disagreeing on fossil fuel and
948	atmospheric growth rate, 18.
949	van Groenigen, K. J., Qi, X., Osenberg, C. W., Luo, Y., & Hungate, B. A. (2014). Faster Decomposition Under
950	Increased Atmospheric CO2 Limits Soil Carbon Storage. Science, 344(6183), 508-509.
951	https://doi.org/10.1126/science.1249534
952	Hajima, T., Tachiiri, K., Ito, A., & Kawamiya, M. (2014). Uncertainty of Concentration-Terrestrial Carbon
953	Feedback in Earth System Models*. Journal of Climate, 27(9), 3425–3445. https://doi.org/10.1175/JCLI-
954	D-13-00177.1

955	Hickler, T., Smith, B., Prentice, I. C., Mjöfors, K., Miller, P., Arneth, A., & Sykes, M. T. (2008). CO2 fertilization
956	in temperate FACE experiments not representative of boreal and tropical forests. Global Change Biology,
957	14(7), 1531–1542. https://doi.org/10.1111/j.1365-2486.2008.01598.x
958	Hiederer, R., & Köchy, M. (2011). Global soil organic carbon estimates and the harmonized world soil database.
959	EUR, 25225, 79.
960	Hungate, B. A., van GROENIGEN, KJ., Six, J., Jastrow, J. D., Luo, Y., de GRAAFF, MA., et al. (2009).
961	Assessing the effect of elevated carbon dioxide on soil carbon: a comparison of four meta-analyses. Global
962	Change Biology, 15(8), 2020–2034. https://doi.org/10.1111/j.1365-2486.2009.01866.x
963	Huntingford, C., Burke, E. J., Jones, C. D., Jeffers, E. S., & Wiltshire, A. J. (2022). Nitrogen cycle impacts on CO $_{2}$
964	fertilisation and climate forcing of land carbon stores. Environmental Research Letters, 17(4), 044072.
965	https://doi.org/10.1088/1748-9326/ac6148
966	Huntzinger, D. N., Schwalm, C., Michalak, A. M., Schaefer, K., King, A. W., Wei, Y., et al. (2013). The North
967	American Carbon Program Multi-Scale Synthesis and Terrestrial Model Intercomparison Project – Part 1:
968	Overview and experimental design. Geoscientific Model Development, 6(6), 2121–2133.
969	https://doi.org/10.5194/gmd-6-2121-2013
970	Huntzinger, D. N., Michalak, A. M., Schwalm, C., Ciais, P., King, A. W., Fang, Y., et al. (2017). Uncertainty in the
971	response of terrestrial carbon sink to environmental drivers undermines carbon-climate feedback
972	predictions. Scientific Reports, 7(1), 4765. https://doi.org/10.1038/s41598-017-03818-2
973	Huntzinger, D. N., Schaefer, K., Schwalm, C., Fisher, J. B., Hayes, D., Stofferahn, E., et al. (2020). Evaluation of
974	simulated soil carbon dynamics in Arctic-Boreal ecosystems. Environmental Research Letters, 15(2),
975	025005. https://doi.org/10.1088/1748-9326/ab6784
976	Jian, J., Vargas, R., Anderson-Teixeira, K., Stell, E., Herrmann, V., Horn, M., et al. (2020). A restructured and
977	updated global soil respiration database (SRDB-V5) (preprint). Data, Algorithms, and Models.
978	https://doi.org/10.5194/essd-2020-136
979	Jian, J., Bailey, V., Dorheim, K., Konings, A. G., Hao, D., Shiklomanov, A. N., et al. (2022). Historically
980	inconsistent productivity and respiration fluxes in the global terrestrial carbon cycle. Nature
981	Communications, 13(1), 1733. https://doi.org/10.1038/s41467-022-29391-5

982	Jiang, M., Medlyn, B. E., Drake, J. E., Duursma, R. A., Anderson, I. C., Barton, C. V. M., et al. (2020). The fate of
983	carbon in a mature forest under carbon dioxide enrichment. Nature, 580(7802), 227-231.
984	https://doi.org/10.1038/s41586-020-2128-9
985	Jones, C. D., Arora, V., Friedlingstein, P., Bopp, L., Brovkin, V., Dunne, J., et al. (2016). C4MIP – The Coupled
986	Climate-Carbon Cycle Model Intercomparison Project:experimental protocol for CMIP6. Geoscientific
987	Model Development, 9(8), 2853–2880. https://doi.org/10.5194/gmd-9-2853-2016
988	King, J. S., Hanson, P. J., Bernhardt, E., DeAngelis, P., Norby, R. J., & Pregitzer, K. S. (2004). A multiyear
989	synthesis of soil respiration responses to elevated atmospheric CO2 from four forest FACE experiments.
990	Global Change Biology, 10(6), 1027–1042. https://doi.org/10.1111/j.1529-8817.2003.00789.x
991	Konings, A. G., Bloom, A. A., Liu, J., Parazoo, N. C., Schimel, D. S., & Bowman, K. W. (2019). Global satellite-
992	driven estimates of heterotrophic respiration. Biogeosciences, 16(11), 2269–2284.
993	https://doi.org/10.5194/bg-16-2269-2019
994	Koven, C. D., Lawrence, D. M., & Riley, W. J. (2015). Permafrost carbon-climate feedback is sensitive to deep soi
995	carbon decomposability but not deep soil nitrogen dynamics. Proceedings of the National Academy of
996	Sciences, 112(12), 3752–3757. https://doi.org/10.1073/pnas.1415123112
997	Koven, C. D., Hugelius, G., Lawrence, D. M., & Wieder, W. R. (2017). Higher climatological temperature
998	sensitivity of soil carbon in cold than warm climates. Nature Climate Change, 7(11), 817-822.
999	https://doi.org/10.1038/nclimate3421
1000	Kuzyakov, Y., Horwath, W. R., Dorodnikov, M., & Blagodatskaya, E. (2019). Review and synthesis of the effects
1001	of elevated atmospheric CO2 on soil processes: No changes in pools, but increased fluxes and accelerated
1002	cycles. Soil Biology and Biochemistry, 128, 66-78. https://doi.org/10.1016/j.soilbio.2018.10.005
1003	Lemordant, L., Gentine, P., Swann, A. S., Cook, B. I., & Scheff, J. (2018). Critical impact of vegetation physiology
1004	on the continental hydrologic cycle in response to increasing CO ₂ . Proceedings of the National Academy of
1005	Sciences. https://doi.org/10.1073/pnas.1720712115
1006	Liu, J., Bowman, K. W., Schimel, D. S., Parazoo, N. C., Jiang, Z., Lee, M., et al. (2017). Contrasting carbon cycle
1007	responses of the tropical continents to the 2015–2016 El Niño. Science, 358(6360).
1008	https://doi.org/10.1126/science.aam5690

1009	Liu, J., Baskaran, L., Bowman, K., Schimel, D., Bloom, A. A., Parazoo, N. C., et al. (2021). Carbon Monitoring
1010	System Flux Net Biosphere Exchange 2020 (CMS-Flux NBE 2020). Earth System Science Data, 13(2),
1011	299–330. https://doi.org/10.5194/essd-13-299-2021
1012	Lovenduski, N. S., & Bonan, G. B. (2017). Reducing uncertainty in projections of terrestrial carbon uptake.
1013	Environmental Research Letters, 12(4), 044020.
1014	Mahecha, M. D., Reichstein, M., Carvalhais, N., Lasslop, G., Lange, H., Seneviratne, S. I., et al. (2010). Global
1015	Convergence in the Temperature Sensitivity of Respiration at Ecosystem Level. Science, 329(5993), 838-
1016	840. https://doi.org/10.1126/science.1189587
1017	Martin, T. A., Hinckley, T. M., Meinzer, F. C., & Sprugel, D. G. (1999). Boundary layer conductance, leaf
1018	temperature and transpiration of Abies amabilis branches. Tree Physiology, 19(7), 435-443.
1019	https://doi.org/10.1093/treephys/19.7.435
1020	Melnikova, I., & Sasai, T. (2020). Effects of anthropogenic activity on global terrestrial gross primary production.
1021	Journal of Geophysical Research: Biogeosciences, n/a(n/a), e2019JG005403.
1022	https://doi.org/10.1029/2019JG005403
1023	Norby, R. J., & Zak, D. R. (2011). Ecological Lessons from Free-Air CO2 Enrichment (FACE) Experiments.
1024	Annual Review of Ecology, Evolution, and Systematics, 42(1), 181-203. https://doi.org/10.1146/annurev-
1025	ecolsys-102209-144647
1026	Nottingham, A. T., Meir, P., Velasquez, E., & Turner, B. L. (2020). Soil carbon loss by experimental warming in a
1027	tropical forest. Nature, 584(7820), 234-237. https://doi.org/10.1038/s41586-020-2566-4
1028	Oleson, K. W., Lawrence, D. M., Gordon, B., Flanner, M. G., Kluzek, E., Peter, J., et al. (2010). Technical
1029	description of version 4.0 of the Community Land Model (CLM).
1030	Pachauri, R., & Reisinger, A. (2008). Climate change 2007. Synthesis report. Contribution of Working Groups I, II
1031	and III to the fourth assessment report. Cambridge University Press, Cambridge.
1032	Peylin, P., Bacour, C., MacBean, N., Leonard, S., Rayner, P., Kuppel, S., et al. (2016). A new stepwise carbon cycle
1033	data assimilation system using multiple datastreams to constrain the simulated land surface carbon cycle.
1034	Geoscientific Model Development, 9(9), 3321–3346. https://doi.org/10.5194/gmd-9-3321-2016

1035	Piao, S., Sitch, S., Ciais, P., Friedlingstein, P., Peylin, P., Wang, X., et al. (2013). Evaluation of terrestrial carbon
1036	cycle models for their response to climate variability and to CO2 trends. Global Change Biology, 19(7),
1037	2117–2132. https://doi.org/10.1111/gcb.12187
1038	Poulter, B., Frank, D., Ciais, P., Myneni, R. B., Andela, N., Bi, J., et al. (2014). Contribution of semi-arid
1039	ecosystems to interannual variability of the global carbon cycle. Nature, 509(7502), 600-603.
1040	https://doi.org/10.1038/nature13376
1041	Pugh, T. A. M., Rademacher, T., Shafer, S. L., Steinkamp, J., Barichivich, J., Beckage, B., et al. (2020).
1042	Understanding the uncertainty in global forest carbon turnover. <i>Biogeosciences</i> , 17(15), 3961–3989.
1043	https://doi.org/10.5194/bg-17-3961-2020
1044	Quetin, G. R., Bloom, A. A., Bowman, K. W., & Konings, A. G. (2020). Carbon Flux Variability from a Relatively
1045	Simple Ecosystem Model with Assimilated Data is Consistent with Terrestrial Biosphere Model Estimate
1046	Journal of Advances in Modeling Earth Systems. https://doi.org/10.1029/2019MS001889
1047	Randerson, J. T., van der Werf, G. R., Giglio, L., Collatz, G. J., & Kasibhatla, P. S. (2017). Global Fire Emissions
1048	Database, Version 4.1 (GFEDv4). https://doi.org/10.3334/ornldaac/1293
1049	Regnier, P., Friedlingstein, P., Ciais, P., Mackenzie, F. T., Gruber, N., Janssens, I. A., et al. (2013). Anthropogenic
1050	perturbation of the carbon fluxes from land to ocean. Nature Geoscience, 6(8), 597-607.
1051	https://doi.org/10.1038/ngeo1830
1052	Saatchi, S. S., Harris, N. L., Brown, S., Lefsky, M., Mitchard, E. T. A., Salas, W., et al. (2011). Benchmark map of
1053	forest carbon stocks in tropical regions across three continents. Proceedings of the National Academy of
1054	Sciences, 108(24), 9899–9904. https://doi.org/10.1073/pnas.1019576108
1055	Schimel, D., Pavlick, R., Fisher, J. B., Asner, G. P., Saatchi, S., Townsend, P., et al. (2015). Observing terrestrial
1056	ecosystems and the carbon cycle from space. Global Change Biology, 21(5), 1762-1776.
1057	https://doi.org/10.1111/gcb.12822
1058	Schwalm, C. R., Schaefer, K., Fisher, J. B., Huntzinger, D., Elshorbany, Y., Fang, Y., et al. (2019). Divergence in
1059	land surface modeling: linking spread to structure. Environmental Research Communications, 1(11),
1060	111004. https://doi.org/10.1088/2515-7620/ab4a8a

Schwalm, C. R., Huntinzger, D. N., Michalak, A. M., Schaefer, K., Fisher, J. B., Fang, Y., & Wei, Y. (2020).
Modeling suggests fossil fuel emissions have been driving increased land carbon uptake since the turn of
the 20th Century. Scientific Reports, 10(1), 9059. https://doi.org/10.1038/s41598-020-66103-9
Sellers, P. J., Berry, J. A., Collatz, G. J., Field, C. B., & Hall, F. G. (1992). Canopy reflectance, photosynthesis, and
transpiration. III. A reanalysis using improved leaf models and a new canopy integration scheme. Remote
Sensing of Environment, 42(3), 187–216. https://doi.org/10.1016/0034-4257(92)90102-P
Shi, Z., Allison, S. D., He, Y., Levine, P. A., Hoyt, A. M., Beem-Miller, J., et al. (2020). The age distribution of
global soil carbon inferred from radiocarbon measurements. Nature Geoscience, 13(8), 555-559.
https://doi.org/10.1038/s41561-020-0596-z
Sitch, S., Huntingford, C., Gedney, N., Levy, P. E., Lomas, M., Piao, S. L., et al. (2008). Evaluation of the terrestria
carbon cycle, future plant geography and climate-carbon cycle feedbacks using five Dynamic Global
Vegetation Models (DGVMs). Global Change Biology, 14(9), 2015–2039. https://doi.org/10.1111/j.1365-
2486.2008.01626.x
Smith, W. K., Fox, A. M., MacBean, N., Moore, D. J. P., & Parazoo, N. C. (2019). Constraining estimates of
terrestrial carbon uptake: New opportunities using long-term satellite observations and data assimilation.
New Phytologist, nph.16055. https://doi.org/10.1111/nph.16055
Smith, W. K., Fox, A. M., MacBean, N., Moore, D. J. P., & Parazoo, N. C. (2020). Constraining estimates of
terrestrial carbon uptake: new opportunities using long-term satellite observations and data assimilation.
New Phytologist, 225(1), 105-112. https://doi.org/10.1111/nph.16055
Swann, A. L. S., Hoffman, F. M., Koven, C. D., & Randerson, J. T. (2016). Plant responses to increasing CO2
reduce estimates of climate impacts on drought severity. Proceedings of the National Academy of Sciences
113(36), 10019–10024. https://doi.org/10.1073/pnas.1604581113
Taylor, K. E., Stouffer, R. J., & Meehl, G. A. (2012). An Overview of CMIP5 and the Experiment Design. Bulletin
of the American Meteorological Society, 93(4), 485–498. https://doi.org/10.1175/BAMS-D-11-00094.1
Viovy, N. (2018). CRUNCEP Version 7 - Atmospheric Forcing Data for the Community Land Model. Research
Data Archive at the National Center for Atmospheric Research, Computational and Information Systems
Laboratory. Retrieved from http://rda.ucar.edu/datasets/ds314.3/

1088	Walker, A. P., Beckerman, A. P., Gu, L., Kattge, J., Cernusak, L. A., Domingues, T. F., et al. (2014). The
1089	relationship of leaf photosynthetic traits - Vcmax and Jmax - to leaf nitrogen, leaf phosphorus, and specific
1090	leaf area: a meta-analysis and modeling study. Ecology and Evolution, 4(16), 3218–3235.
1091	https://doi.org/10.1002/ece3.1173
1092	Walker, A. P., De Kauwe, M. G., Bastos, A., Belmecheri, S., Georgiou, K., Keeling, R., et al. (2020). Integrating the
1093	evidence for a terrestrial carbon sink caused by increasing atmospheric CO2. New Phytologist, nph.16866.
1094	https://doi.org/10.1111/nph.16866
1095	Welp, L. R., Keeling, R. F., Meijer, H. A. J., Bollenbacher, A. F., Piper, S. C., Yoshimura, K., et al. (2011).
1096	Interannual variability in the oxygen isotopes of atmospheric CO2 driven by El Niño. Nature, 477(7366),
1097	579–582. https://doi.org/10.1038/nature10421
1098	Wieder, W. R., Bonan, G. B., & Allison, S. D. (2013). Global soil carbon projections are improved by modelling
1099	microbial processes. Nature Climate Change, 3(10), 909–912. https://doi.org/10.1038/nclimate1951
1100	Wieder, W. R., Hartman Melannie D., Sulman Benjamin N., Wang Ying-Ping, Koven Charles D., & Bonan Gordon
1101	B. (2018). Carbon cycle confidence and uncertainty: Exploring variation among soil biogeochemical
1102	models. Global Change Biology, 24(4), 1563-1579. https://doi.org/10.1111/gcb.13979
1103	Worden, J. R., Bloom, A. A., Pandey, S., Jiang, Z., Worden, H. M., Walker, T. W., et al. (2017). Reduced biomass
1104	burning emissions reconcile conflicting estimates of the post-2006 atmospheric methane budget. Nature
1105	Communications, 8(1), 2227. https://doi.org/10.1038/s41467-017-02246-0
1106	Zhu, Z., Piao, S., Myneni, R. B., Huang, M., Zeng, Z., Canadell, J. G., et al. (2016). Greening of the Earth and its
1107	drivers. Nature Climate Change, 6, 791.
1108	
1109 1110	
1111	